POLYTECHNIC UNIVERSITY OF CATALONIA (UPC)

Fluid Dynamic Characterization of Vortex Generators and Two-dimensional Turbulent Wakes

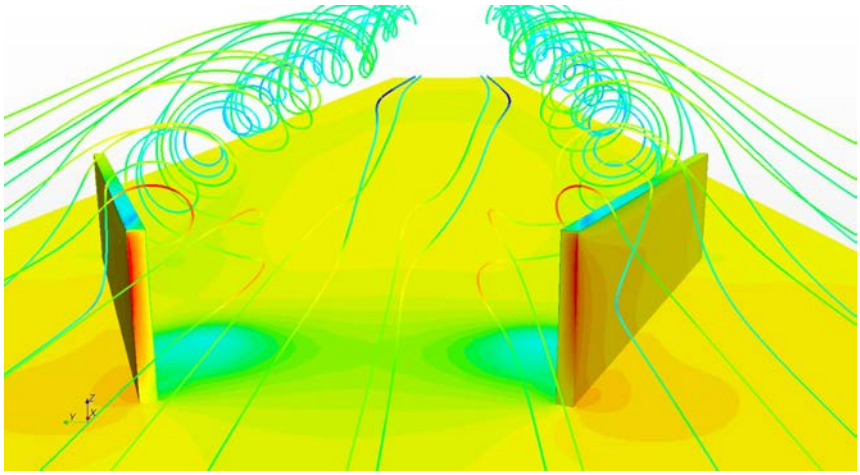

by

Unai Fernández Gámiz

A thesis submitted in partial fulfillment for the degree of Doctor of Philosophy

in the

School of Industrial Engineering of Barcelona (ETSEIB)

October 2013

Declaration of Authorship

I, UNAI FERNANDEZ GAMIZ, declare that this thesis titled, 'FLUID DYNAMIC CHARACTERIZATION OF VORTEX GENERATORS AND TWO-DIMENSIONAL TURBULENT WAKES' and the work presented in it are my own. I confirm that:

- This work was done wholly or mainly while in candidature for a research degree at this University.
- Where any part of this thesis has previously been submitted for a degree or any other qualification at this University or any other institution, this has been clearly stated.
- Where I have consulted the published work of others, this is always clearly attributed.
- Where I have quoted from the work of others, the source is always given. With the exception of such quotations, this thesis is entirely my own work.
- I have acknowledged all main sources of help.
- Where the thesis is based on work done by myself jointly with others, I have made clear exactly what was done by others and what I have contributed myself.

Signed: _____

Date: _____

"Twenty years from now you will be more disappointed by the things you didn't do than by the ones you did do. So throw off the bowlines. Sail away from the safe harbour. Catch the trade winds in your sails. Explore. Dream. Discover."

Mark Twain

POLYTECHNIC UNIVERSITY OF CATALONIA (UPC)

Abstract

School of Industrial Engineering of Barcelona (ETSEIB)

Doctor of Philosophy

by Unai Fernández Gámiz

The main objective of this PhD thesis is a investigation about how the physics of the wake downstream vortex generators in a negligible streamwise pressure gradient flow can be reproduced in the computational simulations. Hence, computational fluid dynamic simulations have been carried out for the analysis of the flow downstream a single vortex generator on a flat plate. In order to evaluate if the computations are able to mimic the induced flow physics of the vortex generators, a test case of a single rectangular vortex generator has been designed and the flow have been numerically simulated and analyzed. Three-Dimensional steady state simulations at low Reynolds number have been performed using EllipSys3D CFD code and the computational results have been compared with experimental data as well as with an analytical model. The BAY source term model for vortex generators has been implemented in the EllipSys3D CFD solver code and it has been validated against experimental observations. Furthermore, a parametric study has been carried out at five different angles of attack of the vortex generator to the oncoming flow in order to evaluate the device angle dependency. The self-similar behaviour and the helical symmetry on the vortex generator induced flow simulations have been also studied.

Finally, a detailed analysis of the equilibrium parameters has been made on a two-dimensional turbulent wake in two different test cases: a twin-plate and a symmetric airfoil (NACA0012). Both cases have been numerically analyzed and the computational results have been compared with experimental observations and with an analytical model for two-dimensional turbulent wakes. Self-similrity on the wake generated by a twin-plate and a symmetric airfoil has been tested and the CFD results match the experimental observations reasonably well.

Acknowledgements

This dissertation is submitted in partial fulfillment of the requirements for obtaining the degree of Doctor of Philosophy (Ph.D.) in Mechanical Engineering by the Polytechnic University of Catalonia (UPC). This research work has been undertaken during the period from September 2010 to September 2013 at the Department of Fluid Mechanics of the Polytechnic University of Catalonia.

This thesis has been carried out under guidance of my supervisors, Professor PhD Eduard Egusquiza Estevez and Associated Professor PhD Clara Marika Velte, to whom I would like to transmit my deepest and sincere gratitude. I wish to thank my main supervisor, E. Egusquiza, for a great guidance and for so many fruitful discussions during this research period. I am indebted to him for giving me the opportunity to carry out the present work. I would also like to declare my deepest thankfulness to C.M. Velte, who believed in me from the beginning. I am indebted to her for her continuous emotional and technical support and great inspiration. When my research life was covered by utter darkness, she was the candle which illuminated my way. Without her support I would never had managed to finish this work.

I am also very grateful to P.E. Réthoré and N.N. Sørensen from DTU-Wind Department for their friendliness and technical support during my outstanding research stay at DTU-Risø Campus in 2011; I still have very good memories of that period in Roskilde. Thanks to E. Zulueta and J. Sancho from University of the Basque Country for so many passionate talks during this research period, benetan ESKERRIK ASKO. Technical and human support provided by IZO-SGI (Txema and Edu), SGIker (UPV/EHU, MICINN, GV/EJ, ERDF and ESF) is also thankfully acknowledged. Thanks to PhD students A. Boyano and I. Ansoategui for their encouragement during those eternal afternoons of hard work, the "cafe-mantas" were the best alleviation for my desperation. Valuable assistant from G.C. Gonzalo and G. Zamorano is also greatly appreciated.

I would also like to mention my close friends Zuriñe, Askoa, Aitziber, Migueltxo and Kindia for so many sweet hugs in the bad moments and for their always very good spirit with me. Thanks to the great friends I found in Copenhagen: Silvia, konrad, Eleni, Crystos, Andreas etc. Thanks again to all of you for making me realize how big is the world and how small is this thesis.

Finally, I am very grateful to my close family for their kindness and understanding. I love all of you brothers, sister, nephwes and sister-in-laws. But in particular, to my father who has been extremely comprehensive and loving during this difficult period of my life, and to my mother who is all the time taking care of me from the sky. Papa, your natural affection has been the best cure of my wounds.

Contents

List of Figures

List of Tables

Abbreviations

VG	**V**ortex **G**enerator
MVG	**M**icro **V**ortex **G**enerator
HAWT	**H**orizontal **A**xis **W**ind **T**urbine
BEM	**B**lade **E**lement **M**omentum
TKE	**T**urbulent **K**inetic **E**nergy
CFD	**C**omputational **F**luid **D**ynamics
RANS	**R**eynolds **A**veraged **N**avier **S**tokes
DES	**D**etached **E**ddy **S**imulations
LES	**L**arge **E**ddy **S**imulations
PISO	**P**ressure **I**mplicit with **S**plitting of **O**perator (CFD solver algorithm)
QUICK	**Q**uadratic **U**pstream **I**nterpolation for **C**onvective **K**inematics
Re	**R**eynolds number
PIV	**P**article **I**mage **V**elocimetry
SPIV	**S**tereoscopic **P**article **I**mage **V**elocimetry
RMSE	**R**oot **M**ean **S**quare **E**rror
SST	**S**hear **S**tress **T**ransport
LDA	**L**aser **D**oppler **A**nemometry
HWA	**H**ot-**W**ire **A**nemometry
POD	**P**roper **O**rthogonal **D**ecomposition
LE	**L**eading **E**dge
TE	**T**railing **E**dge
BL	**B**oundary **L**ayer

Symbols

c	airfoil chord length	m
t	time	s
P	power	W (Js^{-1})
H	vortex generator height	m
u, v, w	mean velocity components in x, y,z directions,respectively	ms^{-1}
x, y, z	cartesian coordinates	
$\omega_r, \omega_\theta, \omega_z$	radial, rotational and axial vorticity,respectively	s^{-1}
r	radial coordinate	
U_{max}	maximum velocity	ms^{-1}
U_∞	freesteam velocity	ms^{-1}
u_z	axial velocity	ms^{-1}
u_θ	azimuthal velocity	ms^{-1}
u_0	vortex convection velocity	ms^{-1}
w_0	center line wake defect velocity	ms^{-1}
l	helical pitch	m
u^+	dimensionless velocity in boundary layers	
y^+	dimensionless wall distance	

ρ	density	kgm^{-3}
μ	viscosity	Nsm^{-2}
ν	kinematic viscosity	$\mathrm{m}^2 s^{-1}$
ν_T	eddy viscosity	$\mathrm{m}^2 s^{-1}$
τ_{ij}	stress tensor	Nm^{-2}
τ_w	wall shear stress	Nm^{-2}
θ	boundary layer momentum thickness	m

β	VG angle of attack	deg
δ	half defect thickness	m
Γ	vortex core circulation	$\mathrm{m}^2 s^{-1}$
ε	vortex core radius	m

Dedicated to my mother and my father. . . the heart of my life.

Part I

Introduction

Chapter 1

Importance of work

According to GWEC (Global Wind Energy Council), a total amount of 238,351 MW of wind power installations was in operation in the world at the end of 2011, of which 96,616 MW in Europe (93,957 MW in the EU-27). In the EU-27, such installed wind capacity would, in a normal year, produce 204 TWh of electricity. There is an offshore wind energy market kicking off and in order to make that market reasonably competitive larger wind turbines are needed. With bigger wind turbine rotors one requires fewer of them and a significant reduction on both capital and operating costs can be reached. But with fewer turbines you have potentially a smaller swept area at wind farm level so you need to compensate for that by equipping the machine with a larger diameter rotor. Current wind turbine design is revolving around the 6 to 7 MW capacity range, with increasingly large rotor diameters.

These large blades, usually pitch regulated, often have a poor aerodynamic performance near the root due to the form and operation limitations. The required structural twist of the rotor blades is very expensive to realize. Therefor, there exists a large potential in increasing the lift for the inner part of a wind turbine blade applying passive flow control devices (e.g. vortex generators) optimally. That is, one can reduce the width of a blade and thus also reduce weight for the same load distribution and power production. The study by Øye [1] (see Figure 1.1) showed that for a particular wind turbine, one could increase lift and thus power production up to 15-25% at normal operating conditions. Making more slender blades is quite important in the process of designing larger cost effective wind turbines where weight and cost are design drivers. Furthermore, surface roughness and leading edge erosion induce local flow separation. This separation has a considerable influence on the aerodynamic performance of the wind turbine blades.

Vortex Generators (VGs) improve the performance of the blades by energizing the boundary layer around the blade and delaying the flow separation (see Figure 1.2).

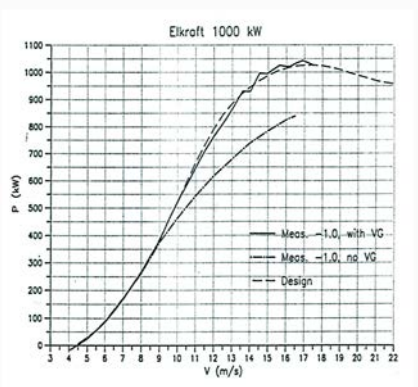

FIGURE 1.1: Influence of Vortex Generators on the performance of the ELKRAFT 1000 kW Turbine [1].

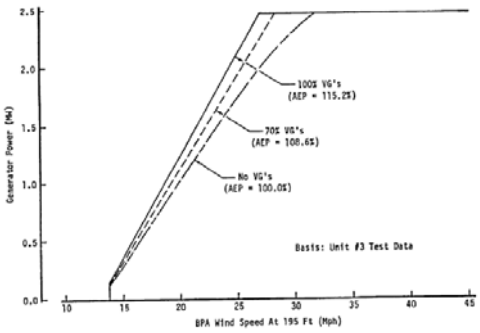

FIGURE 1.2: Effects of Vortex Generators on a 2.5 MW wind turbine power curve [5].

The performance of the entire wind turbine in terms of power, loads and life can be improved by vortex generators implementation. Wind farm projects are characterized by high up-front investment. Thus high wind turbine availability in combination with high energy yield is necessary. Unexpected reparation and power curtailing can have an important effect on the performance of the wind turbine rotor blades. The implementation of VGs on the blades allows the safe, trouble-free performance boosting of existing and new designed wind turbines. Aerodynamic efficiency operation is assured by a careful technical design with a possible noise reduction. VGs have the advantage that they can be added as a post-production fix (retro-fit) to blades that do not perform as expected. The turbulent nature of the wind has a significant effect on the wind turbine blades performance. VGs help to delay the separation of the flow, by delaying stall, and stabilizing the flow. Usually, the most important reason of flow separation is the lack of momentum in the boundary layer. An optimal layout of VGs can delay flow separation by adding momentum from the outer part of the boundary layer to the inner part, by creating vortices. These vortices mix the outer flow with the one inside of the boundary layer region. This also can help to reduce the stall induced noise emissions.

A significant reduction of unsteady aerodynamic effect in the inner part of the blade, can be reached by the installation of vortex generators and consequently the wind turbine rotor lifetime can be increased. Some experiments have shown that with a proper vortex generators layout the lift increases and a stall delay is achieved with a minimal drag penalty [2, 3], see Figure 1.3 .

The most important reason of flow separation is the lack of momentum in the boundary layer, thus usually the primary option in trying to control the flow separation is the installation of vortex generators because they have the advantage of cost-effective and simple to set-up and manufacture as well as highly efficient.

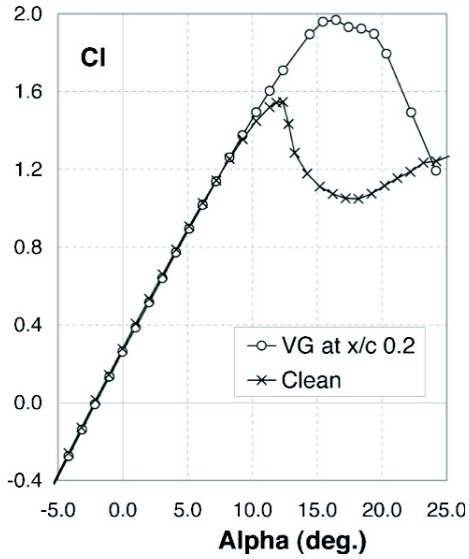

FIGURE 1.3: Effects of Vortex Generators on the performance of DU 97-W-300 airfoil [2]

The mean motivation of the present work is related with the following subjects:

- General need of increased AEP (Annual Energy Production) for a reduced COE (Cost of Energy).
- Particular problems with aerodynamic blade profiles: production dependant on the rugosity (cleanliness) of the blade.
- Up to 7% variation on the energy output of a wind turbine depends on the blades cleanliness.
- Main losses are in the range of 9 to 11 m/s (related to power curve), 80-100% nominal capacity, 30% annual production.
- Geometry of vortex generators and proper location is not easy to define for a blade profile
- Vast range of parameters inherent in the problem: geometry, separation, location, etc.
- Difficulties to develop a simplified design method to quickly obtain optimized parameters for a given blade.
- Improvements to the productivity of existing wind turbines will lead into a decrease on the Cost of Energy.
- Length of the blades limited by weight and load distribution: load reduction for a given power production may lead to length increase.

Chapter 2

State of the art

2.1 Vortex Generators

A Vortex Generator (VG) is a passive flow control device which modifies the boundary layer fluid motion bringing momentum from the outer flow region into the inner flow region of the wall bounded flow. This may be a beneficial approach in flow with adverse pressure gradients, see Figure 2.1 for an example. Through this transfer of energy, the momentum of the near wall region is increased at the same time as the boundary layer thickness is decreased, which in turn causes the separation of the flow to be delayed, Rao *et al.* [6]. Transferring momentum towards the near wall region, i.e. increasing the velocity in the inner region, leads to an increase in the wall shear stress, see Gad-el-Hak [7]. Also for turbulent boundary layers, the wall shear stress is null or close to, under stall conditions. Lin *et al.* [8] showed the Drag reducing and the Lift increasing effect of sub boundary layer VGs.

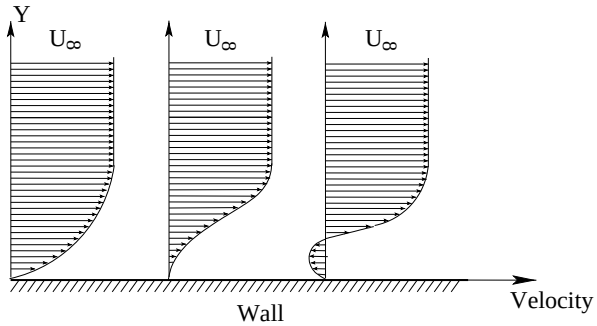

FIGURE 2.1: Boundary layer profile development on a flat plate with an adverse pressure gradient $\frac{\partial p}{\partial x} > 0$.

These devices are usually triangular or rectangular vanes inclined at an angle to the incoming flow. These generators are usually dimensioned in relation to the local boundary

layer thickness to allow for the best interaction between the generated vortex wake and boundary layer, and are usually placed in groups of two or more upstream of the flow separation area, Anderson [9]. The VG generally functions, as its name suggests, by generating streamwise vortices, as sketched in Figure 2.2. Vortex Generators have been investigated for more than fifty years in applied aerodynamics on airplane wings, Taylor [10–12]. These passive vanes have a wide range of engineering applications but they are generally used in flow separation control, mixing and heat transfer applications.These aerodynamic devices generate longitudinal vortices, causing overturning of the near wall flow through macro motions [13]. VGs are designed to re-energize the boundary layer by inducing momentum transfer between the free stream velocity and the near wall region.

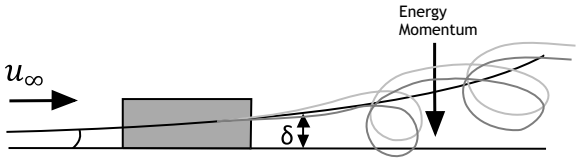

FIGURE 2.2: Boundary layer motion alteration by a rectangular Vortex Generator.

Research on Vortex Generators mounted on a flat plate has previously occupied several researchers, Lin *et al.* [14]. Later investigations at moderate Reynolds number made by Kerho *et al.* [15] with vortex generators used to control laminar separation bubbles, showed a significant drag reduction. Also Lin *et al.* [16] saw the Drag reducing and the Lift increasing effect of VGs smaller than the boundary layer thickness. Wendt *et al.* [17] investigated an array of VGs experimentally where the VGs were arranged to generate counter rotating vortices.

Vortex Generators are frequently applied on wind turbine blades with the aim to delay or prevent separation of the flow and to decrease roughness sensitivity of the blade. They are usually mounted in a spanwise array on the suction side of the blade and have the advantage that they can be added as a post-production fix to blades that do not perform as expected. Vortex Generators extend the lift curve by suppressing turbulent separation. This delay of turbulence separation leads to an increased maximum lift and increased stall angles. An overview of different airfoils with several VG options is listed in van Rooij and Timmer [2]. So, adding VGs in wind turbine blades is a cost-effective and practical solution to improving the performance of a rotor, Schubauer *et al.* [18] and Bragg *et al.* [19].

Later, Godard *et al.* [20] designed a model experiment consisting of a bump in a boundary layer wind tunnel, which mimics the adverse pressure gradient on the suction side of an airfoil at the verge of separation. In that experiment, a parametric study was carried

our in order to obtain the optimal lay-out of the vortex generators using a combination of Particle Image Velocimetry and wall shear stress measurements.. In the work carried out by Velte [3] a detailed study of the longitudinal vortical structures generated by vortex generators was made. In this work several wind tunnel experiments were performed. The flow was recorded using Stereoscopic Particle Image Velocimetry in cross-planes at various positions downstream of the vane. The results of this work showed that at low Reynolds number the device induced vortices possess helical symmetry. Further, their ability to control separated flow and the downstream evolution over a circular sector was studied. For validation of the computational results, the analytical VG model and experimental results presented in the thesis work of Velte [3] is used.

According to [21], the optimal geometric size of the vortex generators varies with the flow it encounters and the needed type of flow modification. In the case of wind rotor blades, it is usually the inner part of the blade that operates in stall conditions, i.e. at high angles of attack to the incoming flow. Stall-delaying VGs are typically mounted between 10-30% of the chord from the leading edge. On wind turbine rotors, VGs are usually fixed at the inboard part of the blades. The effect of VGs in a 1 MW and 2.5 MW wind turbines was investigated by Øye [1] and Miller [5], respectively, where a comparison between the measured power curve on a wind turbine with and without VGs showed empirically that VGs can be applied successfully, increasing the output power for nearly all wind speeds.

2.2 The BAY Model

In order to design a wind turbine blade, and to optimize the position of the VGs on the blade, Computational Fluid Dynamics (CFD) tools can be used. However, modelling the fully-meshed VGs on a full rotor computation becomes prohibitively expensive. Indeed, the Vortex Generator size is often similar to the boundary layer thickness and many small cells are needed in the VG geometry in order to obtain a reliable modelling of the flow. An alternative way of modelling VGs in CFD is to model the influence of the vortex generator on the boundary layer using body forces. In that sense, Bender E.E., Anderson B.H. and Yagle P.J. [22] presented a model for simulating the vane vortex generators without the necessity to define the VG geometry in the mesh. This model avoids the need of generating large and complex grids around the vane geometry by introducing a source term in the discretized momentum and energy equations. Recently, a new vortex generator model called jBAY was introduced by Jirásek [23] for simulations of flow systems with VG arrays. The jBAY model is based on the lifting force theory of [22] but with an improved technique for defining the model control points.

The Bay model is promoted as a high efficiency tool for CFD computations and might be useful for certain applications by the implementation in different in-house and commercial codes.

2.3 Self-similarity and wake equilibrium parameters

Research of the flow field near the trailing edge of submerged bodies has attracted significant interest of researchers over the years. The free turbulent mixing procedure is an inevitable and vital process in numerous realistic phenomena of aerodynamics, Townsend [24], Harsha [25] and Patel *et al.* [26]. Prabhu et al [27] and Narasimha *et al.* [28] conducted some experiments on plane turbulent wakes undergoing transition from an initial equilibrium state to a different final one. These experiments showed evidence of self-similar behaviour of the wake behind different wake generators. Later, Hebbar [29] and Wygnanski *et al.* [30] investigated the boundary layers and wakes on various wake generators where detailed measurements of two-dimensional profiles of static pressure, mean velocity, turbulence intensity and Reynolds shear stress were analyzed. Fernández-Gámiz *et al.* [31] and Velte [4] also investigated numerically and experimentally the self-similar manners of the wake on a rectangular vortex generator on a flat plate.

A flow is said to be self-preserving if solutions to its dynamical equations and boundary conditions exist for which, throughout the evolution of the wake, all dynamical parameters have the same relative value at the same relative position, George [32]. These parameters are sketched in Figure 2.3, where U_∞ is the free stream velocity, u the axial velocity and u_0 the convection velocity. The variables y and x are the characteristic shear-layer width and the velocity scale for each plane position, respectively. Therefore, according to Narasimha *et al.* [28], an equilibrium wake state is defined as one in which the mean velocity and the turbulent stresses exhibit similarity with identical length and velocity scales.

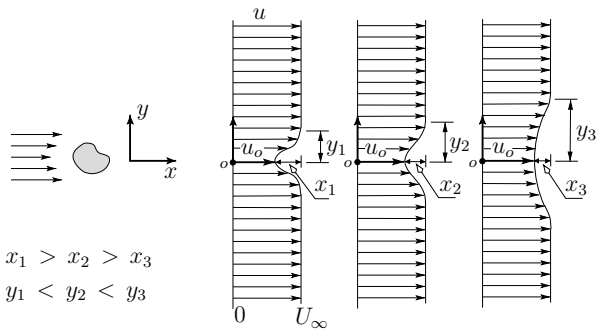

FIGURE 2.3: Wake development behind a body showing the self-preserving parameters.

Self-similarity is a state of self-preservation across scales. For jets and wakes this classically means that the development of the streamwise velocity profiles in the streamwise direction collapse for all positions if scaled correctly according to the theory presented, e.g., by White [33]. Figure 2.3 illustrates the wake velocity profile downstream of a body at several positions behind a body. Self-similarity occurs when the velocity profiles can be brought into congruence by simple scale factors which depend on only one of the variables. A consequence of self-preservation is that the dynamical equations become independent of that variable and thereby reduced by one variable in their functional dependence. This means effectively that one velocity profile is sufficient to describe the entire developed wake using the scaling parameters for the velocity and jet/wake width. Since self-preservation reduces the governing equations to ordinary differential equations, a higher benefit is reached if the original equations are two-dimensional or axisymmetrical, [32]. Thus implies that the flow has reached a kind of equilibrium where all of its dynamical influences evolve together and no extra relative dynamical readjustment is required. The full concept of full preservation means a significant issue in turbulence theory and George [32] investigated that several kinds of states are possible. In particular, the flows can be fully, partially and locally self-preserving depending on the turbulence moments and/or certain scales.

In the present study CFD simulations have been carried out by EllipSys3D CFD Code (Michelsen [34] and Sørensen [35]) and StarCCM+ (www.cd-adapco.com), and compared with experiment data, where several test cases were performed for a relevant and reliable comparison. Particulary, the mean flow velocity profiles of the wake behind a twin-plate and behind a NACA 0012 airfoil were investigated in the sense of wake equilibrium and self-similarity.

The main objective of this work is to investigate how well the simulations can reproduce the self-similar behaviour of the flow and if the same analytical model can be applied. Using this model, parametric studies can be significantly reduced and, furthermore, reliable simulations can substantially reduce the costs of the parametric studies themselves.

Chapter 3

Objectives

The main objective of this PhD thesis is to investigate how the physics of the wake behind vortex generators in a negligible streamwise pressure gradient flow can be reproduced in the CFD simulations. Different computational models have been performed to investigate how well they reproduce the measured physics. Therefore, computational fluid dynamic simulations CFD have been carried out with different codes for the analysis of the flow. In order to evaluate the induced flow effect of the vortex generators, both incident and actuated flow have been numerically simulated and analyzed. Three-Dimensional steady state RANS simulations were performed using EllipSys3D CFD code and the computational results were compared with experimental data.

Additionally, plane turbulent wakes behind wake generators of different shapes have been studied by numerical simulations. Two different wake generators were studied, a twin-plate and a symmetric airfoil NACA0012. Both cases were compared with wind tunnel experimental results. An analytical model was also applied to check the self-similarity and the equilibrium state parameters of the wakes.

The most important goals of this project are:

- Confirmation of the fluid dynamical characterization of the flow behind vortex generators in numerical flow simulations.
- Computational analysis of the effect of vortex generators on the boundary layer separation on a flat plate test case.
- Implementation of the BAY model for a single rectangular vortex generator on a flat plate into EllipSys CFD Code.

- A qualitative and quantitative comparison of different vortex generators models, which will give recommendations for models and for parameters choice, and validation of the results by comparing with experimental data.
- Analysis of the self-similar behaviour of the wake of a single rectangular VG computational simulations as well as the helical symmetry of the main vortex generated by a single vortex generator on a flat plate.
- Two-dimensional numerical analysis of the wake equilibrium parameters and self-similarity behind different wake generator shapes.

Chapter 4

Outline of Thesis

This thesis has been divided into five main parts:

PART I: Introduction.

PART II: Analytical and computational Vortex Generators Models.

PART III: Testing of Self-similarity and Helical Symmetry on Vortex Generator Flow Simulations.

PART IV: Self-similarity and Wake Equilibrium Analysis on Two-dimensional Turbulent Wakes.

PART V: Summary and Future Work.

PART I. In this part, the importance of this research as well as the main motivation to carry out such work is presented. An extensive description of the state of the art of vortex generator models is presented with strong emphasis on wind turbine applications. Further, a detailed explanation of self-similarity and two-dimensional turbulent wake equilibrium is given.

PART II. The three chapters of this part comprise the background theory applied in this thesis. In this part there is a detailed description of the vortex generator models used in this research: the fully mesh-resolved VG model and the Actuator VG model (AcVG). The computational results have been compared with the wind tunnel experiments carried out by Velte [3] as well as with the analytical model of [36], as a validation tools of the computations. The AcVG model is based on the implementation of the BAY model into the EllipSys CFD ([34, 35]) code, as described in *Chapter 5*, and it was performed in conjunction with N.N. Sørensen and P.E. Réthoré. Finally a parametric study of the device angle dependency of a single vortex generator on a flat plate is described in *Chapter 7*. Four different angles of attack have been selected for this parametric study: $\beta = 20°, 25°, 30°$ and $35°$.

PART III. This part is the foundation of the current thesis. A computational analysis of self-similarity on a single rectangular vortex generator wake in a negligible streamwise pressure gradient flow has been made. The simulations were able to capture the helical symmetry of the vortex generator wake with good accuracy when comparing with the experimental data and theoretical model. A very detailed description of the downstream evolution of the helical parameters in the computations is presented in *Chapter 8* and compared with experimental results.

All the computational simulations of PART II and PART III have been made in the THYRA Cluster at DTU-Risø Campus in Roskilde, Denmark, by the EllipSys CFD code during a research stay of the respondent in that institution in 2011. All the experimental data of PART II and PART III have been provided by Clara M. Velte.

PART IV. This part contains an overview of the self-similar behaviour and wake equilibrium parameters of two different cases: a twin-plate and a symmetric airfoil. *Chapter 9* describes the numerical simulations of the main equilibrium parameters on a twin-plate two-dimensional turbulent wake. The computational results have been compared with the measurements carried out in Sreenivasan *et al.* [37] as well as with the analytical model for two-dimensional turbulent wakes of Narasimha *et al.* [28]. In *Chapter 10* numerical simulations on a symmetric airfoil have been performed in order to analyze the main equilibrium parameters of the NACA0012 airfoil wake. The results have been compared with the experimental ones made by Hebbar [29] and with the previously mentioned analytical model. In addition, a complete analysis on the computational results has been carried out in both test cases (twin-plate and symmetric airfoil) in order to verify the self-preserving behaviour of the wake.

All the computational simulations of this part have been run on the ARINA Cluster at UPV-EHU Bizkaia Campus in Leioa, by the StarCCM+8 double precision CFD code provided by CD-Adapco.

PART V. A summary of the contributions of this work is given in this part. The general conclusions of this thesis are described in this chapter as well as some recommendations for future investigations. Some suggestions are also provided to continue this line of research.

Part II

Vortex Generators Models

Chapter 5

Analytical and Computational Vortex Generator Models Description

Computational fluid dynamics is a very common tool used to predict wind turbine blade aerodynamic performance. Since, VGs have the potential to improve the blade performance, it would be desirable to include the influence of the VGs in the computations. However, in terms of both the mesh generation effort and computational time, the simulations with mesh-resolved VG models are extremely expensive. Therefore, in order to decrease the effort in grid generation and the computational time, it would be very helpful to model the effects of the VGs without including their geometry in the mesh.

Bender *et al.*[22] developed a source term model based on the Joukowski lift theorem and thin airfoil theory, called the BAY model. This model was presented for simulating vane Vortex Generators in a finite volume the Navier-Stokes code that eliminates the requirement to define the geometry in the mesh. For the calibration of the model, a test case was created by [22] for comparison of the results with a modelled VG and the gridded VG. This test case consisted in a pipe with 24 VGs mounted circumferentially in a co-rotating configuration. The study showed to promising results. Subsequently, a new improved version of the BAY model was developed by A. Jirsek [23], called jBAY model. This new version was based on the lift force theory of [22] and provided a more capable method for simulating the flow with rows of VGs. Jirsek [23] used a simplified technique for defining the model control points, so in this way it was easier to implement the model and the results were more accurate. The model was tested with a single VG on a flat plate, in an S-Duct air intake in a high-lift wing configuration. The results showed very good agreement between experimental data and CFD computations. Afterwards, an

empirical model of VGs was incorporated into the Wind-US Navier-Stokes CFD code by Dudek [38] and in 2011 a simplified implementation was developed by Dudek [39]. With the implementation of the BAY model in the CFD code, the effects of the VGs using fine mesh are simulated by adding lift forces in the region of cells at the VG position. With this simplification the reduction of mesh cells and computational time could be relevant in comparison with the mesh-resolved VG, Fernández *et al.* [40].

5.1 Computational models description

Four VG cases have been employed in this work for a detailed comparison, both qualitatively and quantitatively. In order to carry out this comparison, a test case based on a single VG in a flat plate was designed. The structure of this work has been organized according to Figure 5.1.

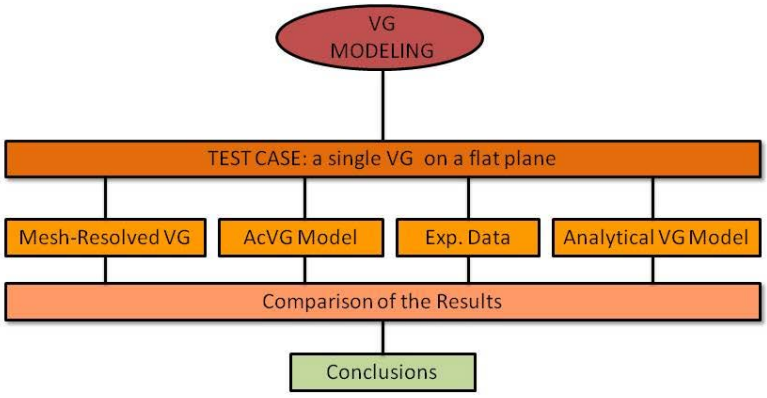

FIGURE 5.1: Test case lay-out.

The computations of the two numerical models, mesh-resolved VG and AcVG model, were performed using the EllipSys CFD code Michelsen [34] and Sørensen [35] (for more information about this solver CFD code is provided in Appendix A), which is a structured finite-volume CFD package for the numerical simulations of flows using Reynolds-Averaged Navier-Stokes equations. Additional information about RANS equations is provided in Appendix B.

These two numerical models are compared with the results of a wind tunnel experiment. In this experiment, a parametric study was performed over a single vane placed on the test section wall in a low-speed wind tunnel. The flow was recorded using Stereoscopic Particle Image Velocimetry, in cross-planes at various positions downstream of the vane, providing instantaneous three-component realizations throughout the measurement plane. This enables an overview of the averaged downstream development of

the wake, including both velocity field and streamwise vorticity, suitable for comparison with computations. The experimental conditions and setup are as described in *Section 5.2*.

Finally, an analytical model of the primary vortex is considered in the context of the two CFD models and the wind tunnel experiment. The model described in Velte [3], which can reduce the complex measured flow to merely four parameters (circulation, convection velocity, vortex core radius and pitch), enables also a quantitative comparison. More detailed information about this analytical model is provided in *Section 5.3*.

In every test case the measurements have been conducted in a spanwise plane, in a plane normal to the flat plate, positioned five VG heights downstream of the vortex generator.

5.1.1 Mesh-resolved vortex generator model

This numerical test case consists of a single VG on a flat plate and the computational domain has been defined with the following dimensions, normalized with the VG height, Figure 5.2. The flow domain length is 30 times the VG height and the height is 10 times. The flow domain width is 32 times the VG height in order to capture the generated vortex. The boundary conditions of the computational domain were defined as velocity inlet for the oncoming flow and pressure outlet for the outgoing flow. A wall no-slip condition was chosen for representing the test section floor.

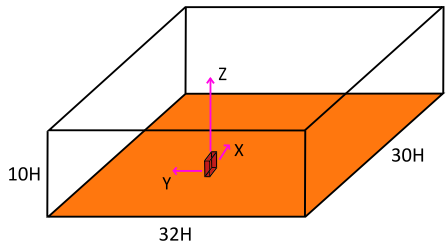

FIGURE 5.2: Computational domain of mesh-resolved VG model.

The dimensions of the rectangular VG are set using an aspect ratio with a length of two times the VG height, see Figure 5.3. The thickness of the vane is constant and with no sharp edges. A boundary layer develops over the flat plate, forced by the viscous interaction between the wall and the flow. The VG was positioned on the flat plate in such way that the boundary layer thickness at this location is equal to the VG height.

The angle of attack to the oncoming flow is set to 20 degrees, (Figure 5.4). The Shear Stress Transport SST turbulence model has been chosen due to its ability to solve swirling flows, see Liu *et al.* [41].

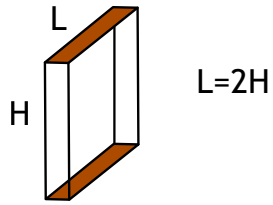

FIGURE 5.3: VG dimensions.

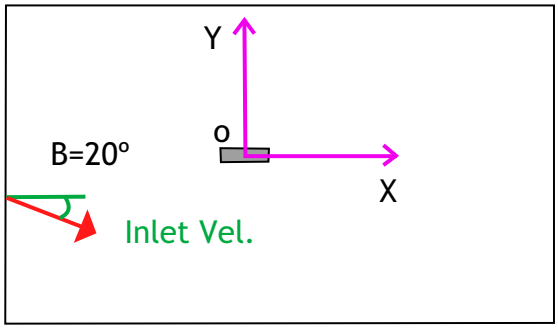

FIGURE 5.4: Angle of attack.

The Reynolds Number based on the VG height H is:

$$Re = \frac{\rho U_\infty H}{\mu} \tag{5.1}$$

where ρ is the density, μ the viscosity and U_∞ the free stream velocity. The computational setup of the fully-meshed VG model consists in a block structured mesh of 18 million cells with the largest part of them used to capture the vortex generated downstream the VG, see Figure 5.5. For a mesh dependency study, the procedure has been achieved by using the Richardson Extrapolation Method, Richardson et al [42] and Stern et al [43]. Three parameters are calculated in the Richardson Extrapolation: p, R and RE, which are the order of accuracy, the error ratio and the extrapolated solution, respectively. A fine, medium and coarse mesh are defined with the corresponding mesh sizes *h1*, *h2* and *h3* (see Appendix C for more information about the procedure). A mesh dependency of less than 5% has been detected in the axial velocity. In order to resolve the boundary layer, cell clustering has been used close to the wall and the dimensionless distance from the wall is less than 2 ($y^+ < 2$), as the SST turbulence model requires.

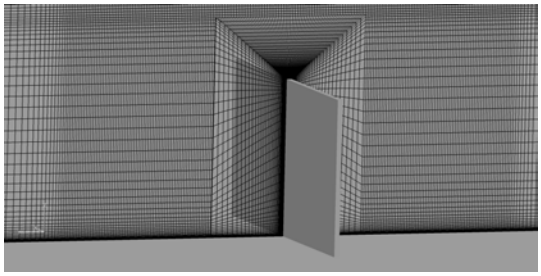

FIGURE 5.5: Mesh Section on the VG.

5.1.2 Actuator vortex generator model

On a wind turbine, VGs are often used to improve the performance of the blades by minimizing the effects of the boundary-layer separation and the adverse pressure gradients. So, computational fluid dynamics (CFD) methods are used to simulate the flow and to predict the blade performance. Together with experiments in wind tunnels, it is a very useful tool for parametric studies of VG lay-out, however, these CFD methods are very time consuming in the computations and in generating a high level quality mesh.

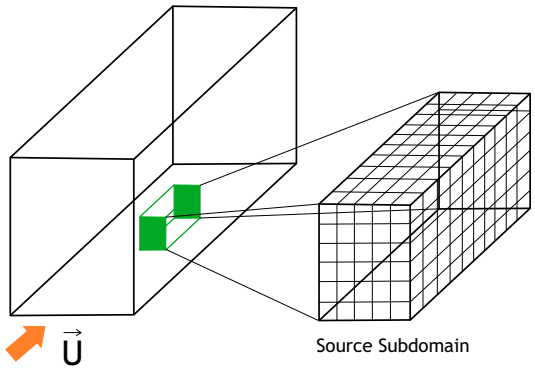

FIGURE 5.6: BAY model source subdomain on a flat plate.

In this work we therefore implement the Actuator Vortex Generator model (AcVG) based on the Bay model, developed by Bender *et al.* [22]. The main idea of the BAY model is to replace the VG geometry by a subdomain at the original VG location and to apply the force distribution in this region, as shown in Figure 5.6.

The BAY model incorporates a source term in the momentum and/or energy equations where VGs are taken in account through the body forces exerted on a fluid:

$$V_i \frac{\Delta(\rho\vec{U})}{\Delta t} = \sum_j F_{Mj} S_j + L_i \tag{5.2}$$

$$V_i \frac{\Delta(\rho E)_i}{\Delta t} = \sum_j F_{Ej} S_j + L_i \tag{5.3}$$

where F_{Mj} is the momentum flux vector through cell face j, F_{Ej} is the energy flux through cell face j, $\vec{U}$ is the local velocity vector, S_j is the area of the cell face j and L_i the force generated by the VG model on a cell. The source term applies a force normal to the local flow direction, parallel to the surface which simulates the side force generated by a VG.

$$L_i = c_{VG} S_{VG} \frac{V_i}{\sum V_i} \alpha \rho U^2 \hat{l} \tag{5.4}$$

The variable U is the local velocity, α is the angle of the incidence of the vane, Vi is the volume of the grid cell and $\sum V_i$ is the sum of the cells where the model is applied. ρ is the local density, S_{VG} is the planform area of the VG, $\hat{l}$ is the unit vector defining the direction of L and c_{VG} is an empirical constant for calibration (a exhaustive explanation about the structure of the BAY model is provided in Appendix D). Therefore, in the Actuator VG model a parametric analysis was performed to determinate a reliable value of the parameter c_{VG} and validated with the mesh-resolved VG model. The Figure 5.7 shows the calibration parameters to determinate optimal value of that for the value of c_{VG}. The total force on the vane found in the mesh-resolved VG model was $f = 3.32\times10^{-2}$ and it corresponds to a c_{VG} value of 2.2.

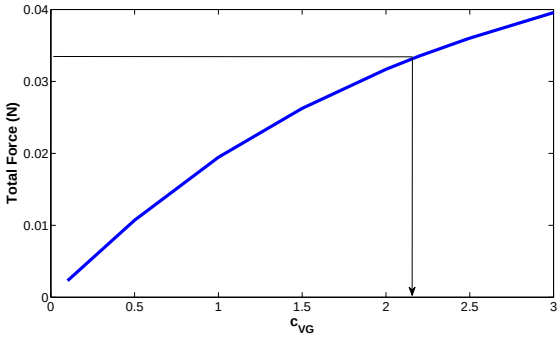

FIGURE 5.7: Calibration of the c_{VG} parameter.

The innovation of this research is that instead of applying forces in all cells of the subdomain, as the BAY model, the force is applied in cells just in the outline of the VG geometry, see Figure 5.8. The forces are applied into the computational domain using the actuator shape model presented in Réthoré *et al.* [44]. The body forces are applied in the domain using a modified Rhie-Chow algorithm presented in Réthoré and Sørensen [45], using the EllipSys CFD code, Michelsen [34] and Sørensen [35]. The Actuator VG model has been designed to be user-friendly. Within the EllipSys CFD code, the user only specifies the following parameters for each VG to be modelled: the cells where the model will be applied and the angle of the incidence of the VG.

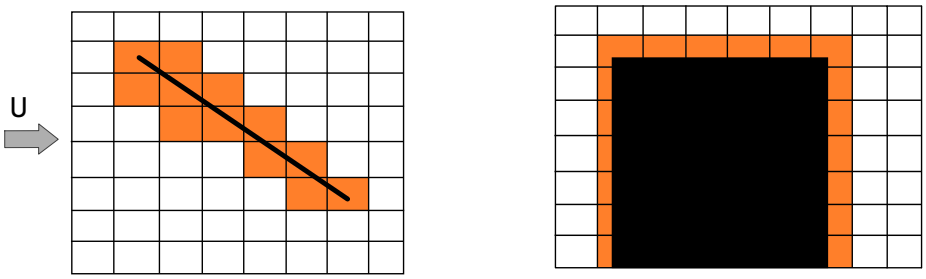

FIGURE 5.8: Cells where the forces are applied. Left panel, top view and right panel, side view

A mesh dependency study for Actuator VG model has been performed with 3 different grid levels and the calculated dimensionless distance is less than 2 ($y^+ < 2$). Results of the fine mesh are compared with the course and medium mesh results, Figure 5.9.

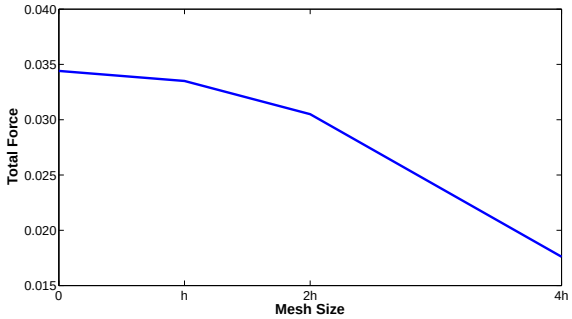

FIGURE 5.9: Mesh Dependency plot.

5.2 Description of the experiments

Consider the test section setup in Figure 5.10. The measurements were carried out in a closed-circuit wind tunnel with an 8:1 contraction ratio and a test section of cross-sectional area 300×600 mm with length 2 m. At the inlet of the test section, a turbulence-generating grid with mesh length 39 mm was situated. The experimental setup is the one of Velte [4]

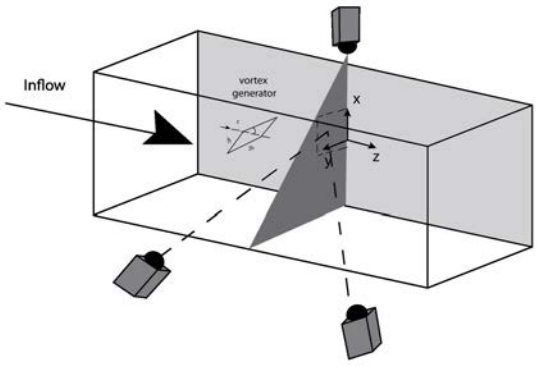

FIGURE 5.10: Schematic illustration of the experimental set-up (inspired in figure 5.2 of [3]).

The experiments were conducted with a variable angle β to the oncoming flow at low-Reynold-number flow, where Re=1700 based on the VG height h=0.025 m and free stream velocity U_∞= 1 ms^{-1}. The wind tunnel speed was obtained by measuring the pressure drop across an orifice plate. The turbulence intensity at the inlet from laser doppler anemometry (LDA) measurements has been found to be 13%. The boundary

layer thickness at the position of the vortex generator has been estimated from LDA measurements to be approximately $\delta_{VG} = 25$ mm. The actuator, as seen in Figure 5.10, is a rectangular vane of the same height as the local boundary layer thickness, $h = \delta_{VG}$, with a length of $2h$. The vortex generator was positioned on a vertical wall in the center of the test section with its trailing edge 750 mm downstream of the inlet grid when it is at zero angle to the mean flow.

The measurements were conducted in a spanwise plane, with plane normal parallel to the test section walls, positioned five device heights downstream of the vortex generator. The measurement plane has been indicated by a dashed line in Figure 5.10.

The SPIV equipment was mounted on a rigid stand and included a double cavity New Wave Solo 120XT Nd-YAG laser (wavelength 532 nm) capable of delivering light pulses of 120 mJ. The pulse width, i.e., the duration of each illumination pulse, was 10 ns. The light-sheet thickness at the measurement position was 2 mm and was created using a combination of a spherical convex and a cylindrical concave lens. The equipment also included two Dantec Dynamics Hi-Sense MkII cameras (1344×1024 pixels) equipped with 60 mm lenses.

5.3 Analytical vortex generator model

The starting point is the classical Lamb-Oseen vortex model;

$$\omega_r = 0; \quad \omega_\theta = 0; \quad \omega_z = \frac{\Gamma}{\pi\varepsilon^2} exp\left(-\frac{r^2}{\varepsilon^2}\right) \tag{5.5}$$

where ω_r, ω_θ and ω_z are radial, rotational and axial vorticity, respectively. Γ is the vortex core circulation, ε the vortex core radius and r the radial coordinate in the cylindrical coordinate system. This simple Lamb-Oseen model merely includes rotation in the plane with plane normal parallel to the axis of the longitudinal vortex. From measurements and computational results however, one can clearly observe an induced velocity in the axial direction, see Velte *et al.* [36]. Similarly to an electrical coil inducing a magnetic field when passing current through the wires, the vorticity lines, which have a helical shape rather than being straight lines parallel to the longitudinal vortex, induce a velocity field.

$$\omega_r = 0; \quad \omega_\theta = r\omega_z/l; \quad \omega_z = \frac{\Gamma}{\pi\varepsilon^2} exp\left(-\frac{r^2}{\varepsilon^2}\right) \tag{5.6}$$

l is the helical pitch, i.e., the period of the helical vorticity lines.

Only a brief description of the analytical model given in the current text. For more details, please see [4, 36]. Helical symmetry on the vortices generated by VGs has previously been shown in [36]. This means that the axial, u_z, and rotational, u_θ, velocities are linearly related:

$$u_z - u_0 = -\frac{r}{l}u_\theta \Longleftrightarrow u_z = u_0 - \frac{r}{l}u_\theta \tag{5.7a,b}$$

(z, θ, r) are the coordinates in a polar coordinate system of the longitudinal vortex where z is parallel to the vortex axis. u_0 is the vortex convection velocity, r the radial coordinate and l the helical pitch of the vorticity lines. Together with the Batchelor vortex model

$$u_\theta(r, \theta, z) = \frac{\Gamma(z)}{2\pi r}\left[1 - \exp\left(-\frac{r^2}{\varepsilon^2(\theta, z)}\right)\right];$$

$$u_z(r, \theta, z) = u_0 - \frac{\Gamma(z)}{2\pi l(\theta, z)}\left[1 - \exp\left(-\frac{r^2}{\varepsilon^2(\theta, z)}\right)\right] \tag{5.8}$$

this allows the generated flow to be described by merely four parameters: vortex core radius $\varepsilon(\theta, z)$, circulation $\Gamma(z)$, convection velocity $u_0(z)$ and helical pitch $l(\theta, z)$, leaving no restrictions on the shape of the vortex core. This model was further expanded to include the downstream vortex development using self-similarity analysis [4] in a low Reynolds number flow with a negligible streamwise pressure gradient. Self-similarity analysis is common for jets, but can conveniently be applied to wakes as well [33]. For the measured time-averaged far wake behavior it is proposed that [4]:

$$\frac{u_z - u_0}{U_\infty - u_0} = \text{fcn}\left(\frac{r}{\varepsilon}\right) \tag{5.9}$$

where the vortex core radius $\varepsilon(\theta, z)$ is chosen as the characteristic width of the wake and U_∞ is the free-stream velocity. Note that $\varepsilon = \varepsilon(\theta, z)$, $l = l(\theta, z)$ and $u_0 = u_0(z)$ are all functions of the vortex axial coordinate z. The self-similarity relation (5.9) should also be compared to the velocity formulation (5.7a), which has been confirmed to apply to the current flow [36], where the left-hand-side corresponds to the left-hand-side numerator in (5.9). A convenient scaling for the azimuthal velocity u_θ is to normalize it by its maximum value, which should occur at the shear layer width [4]. From self-similarity of

both u_z and u_θ, the model presented in [4] can be extended to include the downstream development of the vortices.

The only requirements for a full flow description using this simple model are the size of the vortex core (ε), the circulation (Γ), the helical pitch (l) and the vortex convection velocity (u_0).

Chapter 6

Comparison of the numerical models to experiments and the analytical model

A single Vortex Generator on a flat plate test case has been designed and implemented using two numerical models. The first one is the traditional mesh-resolved VG and the second one, called Actuator Vortex Generator model (AcVG), is based on the lifting force theory of Bender, Anderson and Yagle, the BAY model, which provides an efficient method for computational fluid dynamic (CFD) simulations of flow with VGs, and the forces are applied into the computational domain using the actuator shape model. This AcVG model enables to simulate the effects of the Vortex Generators without defining the geometry of the vortex generator in the mesh and makes it easier for researchers the investigations of different vortex generator lay outs. Both models have been archived by the EllipSys CFD code using Reynold-Average Navier-Stokes (RANS) methods. The results of these two numerical model implementations are compared to experimental results where measurements were carried out in a low speed closed-circuit wind tunnel utilizing Stereoscopic Particle Image Velocimetry (SPIV) with a single vortex generator positioned on a vertical wall in the center of the test section. An analytical model, describing the actual physics of the flow from the measurement results, provides a quantitative comparison for primary vortex based in the helical structure of longitudinal embedded vortex.

The goal is to validate the AcVG model compared with a fully meshed VG, a wind tunnel experiment and an analytical VG model, all of them previously described in *Chapter 5*. The results of the four cases have been compared quantitatively and qualitatively.

Figures 6.1 (a) and (b) show the streamwise velocity iso-contours of the VG wake generated downstream the trailing edge of the VG for the mesh-resolved VG model on the left and for the Actuator VG model on the right, respectively. The inner separation between planes is four times the VG height starting five times the VG height behind the vortex generator.

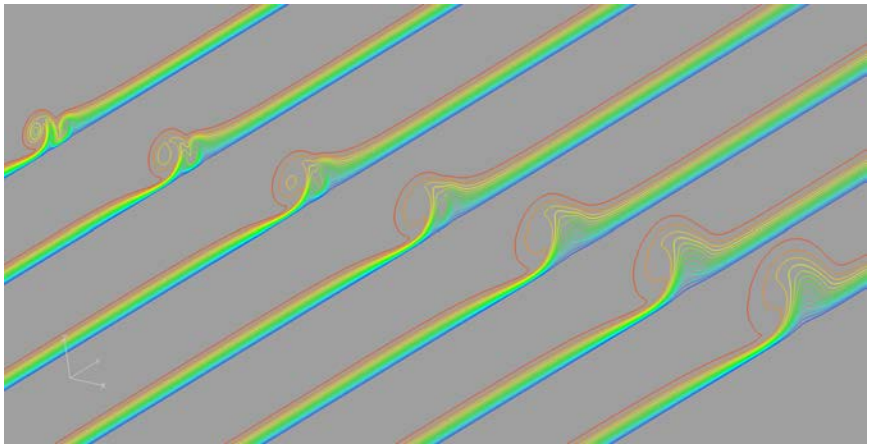

(a) mesh-resolved VG model.

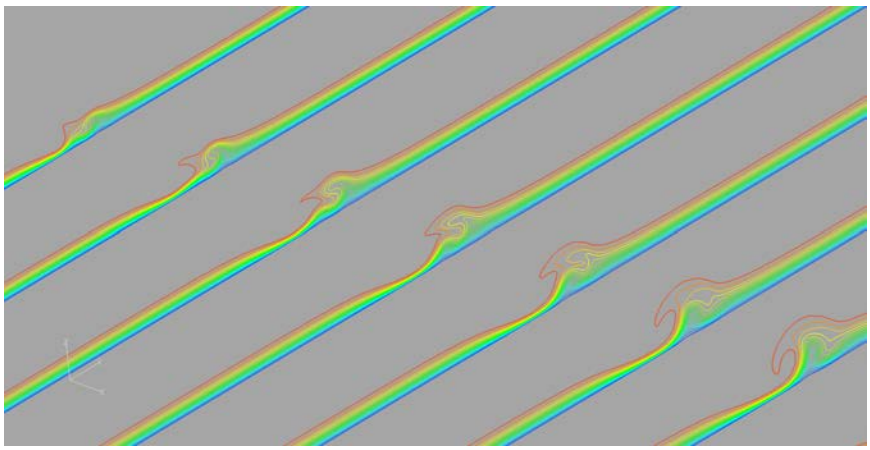

(b) AcVG model

FIGURE 6.1: CFD results of the axial velocity iso-contours of a single VG on a flat plate.

6.1 Qualitative Comparison

For a qualitative comparison between the mesh-resolved VG model and the AcVG model, four parameters have been chosen: pressure, axial velocity, vorticity and turbulent kinetic energy. All of these fields have been taken at the calibration distance of one single plane five VG heights downstream the trailing edge of the VG, as sketched in Figure 6.2, and the results have been plotted in Figure 6.3. Left column represents the results of the mesh-resolved VG computational model and the right column the results of the

Actuator VG model (note the different scales for TKE). Differences are clear in all the parameters. It seems that the main vortex generated by the virtual VG in the case of the AcVG model is not fully developed at the distance of five VG heights behind the trailing edge. The comparison represented in Figures 6.1(a) and (b) could confirm the delay in the primary vortex development. Note that a secondary vortex is visible in in the mesh-resolved VG model, nevertheless in the case of the AcVG model this secondary vortex is not evident.

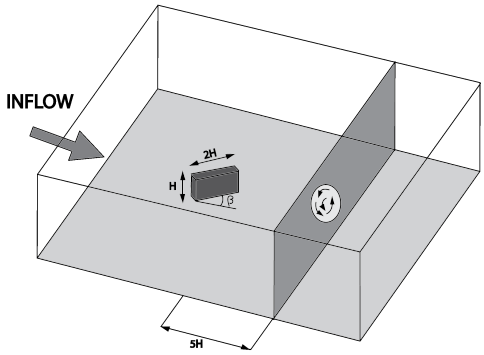

FIGURE 6.2: Plane location where the measurements were conducted.

6.2 Quantitative Comparison

As a quantitative comparison, the analytical model of the primary vortex is considered in the context of the two CFD models (mesh-resolved VG and AcVG models) and the wind tunnel experiments explained in *Section 5.2*. This analytical model described in *Section 5.3* (more details can be found in Velte [3]), reduces the complex flow to four parameters (circulation, convection velocity, vortex core radius and helical pitch) and enables quantitative comparison in addition to the qualitative one.

Figure 6.4 shows the axial u_z (upper) and azimuthal u_θ (lower) velocity profiles for 20 degrees of the device angle extracted along a line parallel to the wall through the center of the primary vortex and located at the calibration plane.

In order to analyse the quantitative differences between the results of the four models, the Root Mean Square Error RMSE between the velocity profiles have been calculated.

Figure 6.5 shows the differences between the two numerical models and the experiments and analytical model of the flow, having as a reference the Actuator VG model. Green colour bars illustrate the axial velocity differences and the yellow ones the azimuthal differences for all cases. C1 and C2 represent the mesh-resolved VG and the AcVG model,

Fields for qualitative comparison:

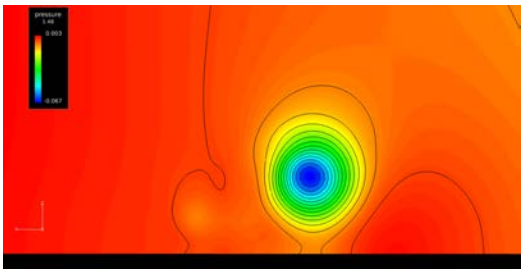

(a) Pressure (scale: -0.067 - 0.003)

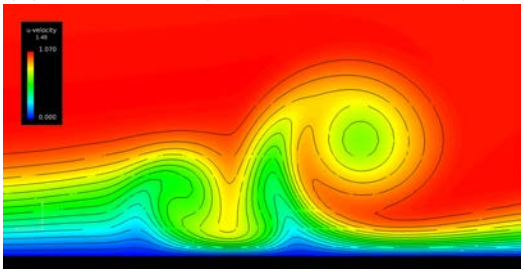

(b) Axial Velocity (scale: 0 - 1.09)

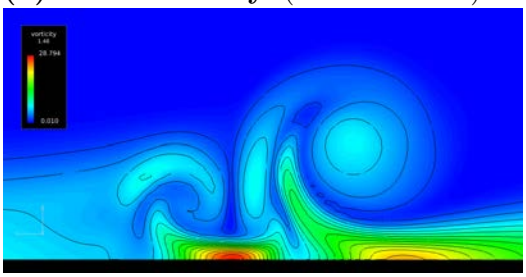

(c) Axial Vorticity (scale: 0 - 28)

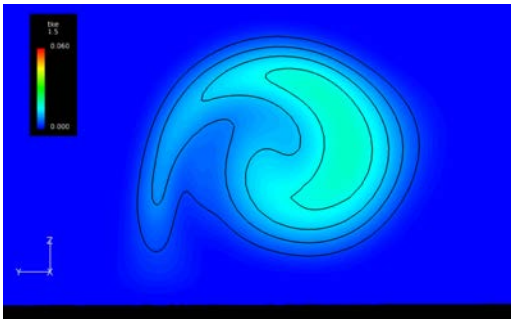

(d) TKE (scale: 0 - 0.06)

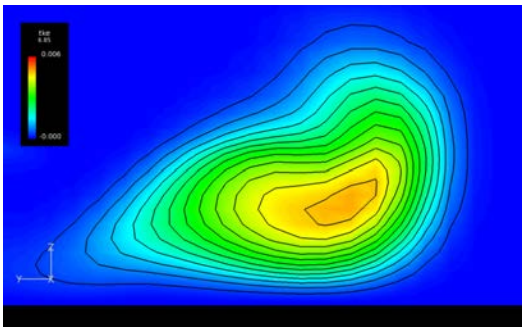

TKE (scale: 0 - 0.006)

FIGURE 6.3: Fields for qualitative comparison. Mesh resolved VG model on the left and AcVG model on the right. (a) Pressure, (b) Axial Velocity, (c) Vorticity, (d) Turbulent Kinetic Energy TKE fields (note the different scales for TKE).

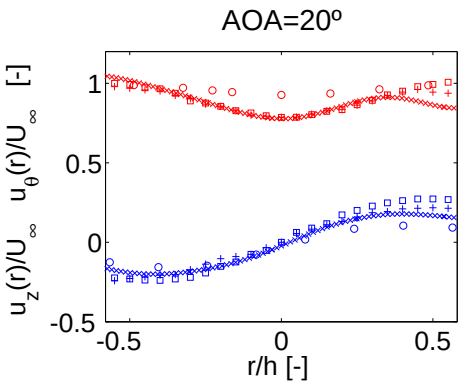

FIGURE 6.4: Comparison of axial and azimuthal velocities normalized by U_∞ of embedded vortices generated by a vortex generator for a device angle of 20 degrees. (x) mesh-resolved VG model, (○) Actuator VG model, (+) Experimental data model, (□) Analytical VG model. Upper values (red colour) are the axial velocity profile u_z and lower (Blue colour) the azimuthal velocity profile u_θ.

respectively. C3 represents experimental data and the analytical model is represented by C4. For example, C2-Ci symbolizes the difference between the AcVG model C2 and the Ci case, which represents the result of one of the other three cases analyzed. The highest difference between the grided model and the actuator model (C2-C1) is in the axial velocity, what is also in concordance with the profiles shown in Figure 6.4.

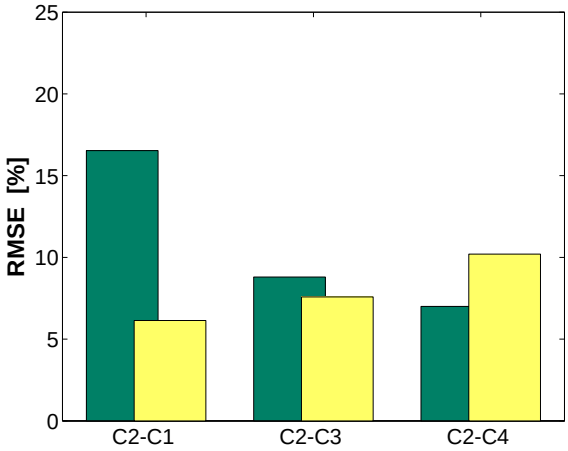

FIGURE 6.5: Root mean square errors in the four cases for the axial (green) and the azimuthal (yellow) velocities. C1, C2, C3 and C4 represent: the mesh-resolved VG model, the AcVG model, the experimental data and the analytical model of *Section 5.3*, respectively.

More bar charts have been illustrated in Figure 6.6 for a quantitative comparison based on the analytical VG model parameters described in *Section 5.3*. These are defined as: vortex core radius (ε), circulation (Γ), helical pitch (l) and convection velocity (u_0). These parameters were measured in a plane normal to the section floor positioned five VG heights downstream and in the spanwise direction, as sketched in Figure 6.2. For

a reliable comparison, the helical pitch pitch and the vortex core radius have been normalized by the corresponding VG height in each case, the convection velocity by the freestream velocity and finally the circulation by $U_\infty h$.

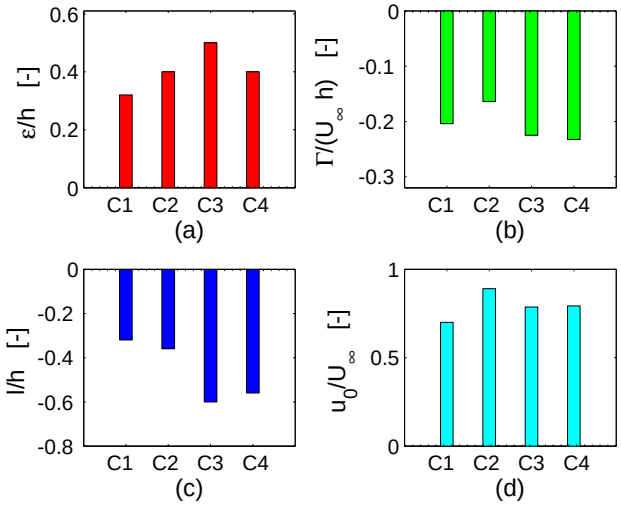

FIGURE 6.6: Comparison charts of the parameters: (a) Vortex radius, (b) Circulation, (c) helical pitch and (d) advection velocity. C1, C2, C3 and C4 represent: the mesh-resolved VG model, the AcVG model, experimental data and the analytical model of *Section 5.3*, respectively.

6.3 Results

Results of the calibrated Actuator VG model have been compared with the mesh-resolved VG model, the experimental data and the Analytical model. Significant differences have been observed between the four cases. The deviations between the values of the Actuator VG model and the values predicted by the analytical model (which were originally fitted to the experimental data) are notable.

Regarding to the computational time, the mesh-resolved VG model time has been estimated to be about three hundred times bigger than the Actuator VG model time. So from the point of view of the computational effort, the efficiency of the AcVG model is much higher than the mesh-resolved VG. Further, a significant reduction in cells is achieved by replacing the detailed VG boundary layer mesh by the new modelling method. This mesh reduction decreases both the VG geometry meshing time and the computational time. These results show that the AcVG and mesh-resolved VG models are qualitatively similar. Once the vortex produced by the mesh-resolved VG is fully developed at around 10 VG heights downstream the trailing edge of the VG, the AcVG model matches reasonably the vortex generated by the mesh-resolved VG model. Some discrepancies are visible in the quantitative comparison, above all in the axial velocity.

It might be because the vortex development at the calibration plane (five VG heights downstream the trailing edge of the vortex generator) is not completed. As the Figure 6.5 shows, the most important divergences of the models in comparison with the Actuator VG model are located in the axial velocity. Furthermore, the values of the helical pitch and the vortex core radius are higher in the Actuator VG model than in the mesh-resolved VG, see Figure 6.6. As previously mentioned, the reason of this deference could be found in the delay of the development of the main vortex in the streamwise direction.

As illustrated in the fields of Figure 6.3(d), significant differences are also visible on the amount of turbulence kinetic energy TKE generated between the fully meshed VG model and the Actuator VG model, which produces less turbulence, as can be expected from this type of source term models. In the mesh-resolved VG methodology, the boundary layer is resolved on the actual VG, which produces a high shear and high turbulence. However, in the volume source approach, e.g. the BAY model, the boundary layers are not resolved, and the high turbulence produced in the boundary layers are thus missing. This argue is in connection with the diferences obserbed in the application of the Actuator Line and the Actuator Disc methodologies described in Troldborg *et al.* [46].

6.4 Conclusions

In conclusion, a new model has been implemented in the EllipSys CFD code and demonstrated that it saves both meshing and computational time. This method could easily be applied for complementing full rotor computation and for conducting parametric studies of the VG layout. The potentially open applications of the Actuator VG model are several. Nonetheless, more investigations are required in order to reach more accurate solutions.

Though acquired in a low Re boundary layer, the flow simulation models are able to qualitatively capture the large scale flow motions, including the secondary perturbing vortex. The vortices are very sensitive to the applied boundary conditions and therefore the flow models used can impact the vortical flow differently, see Okulov [47]. It is surprising that the axial velocity is not predicted as well as the rotational one, which should be much more sensitive to the conditions of the surroundings, see Alekseenko [48]. We can also confirm that the analytical model developed by [36] can be used as a calibration tool for the AcVG model.

For future investigations, it would be highly interesting to investigate if the Actuator VG model calibration is independent of the Reynolds number and the inflow angle.

Chapter 7

Parametric study of the device angle dependency of a single vortex generator in a negligible streamwise pressure gradient flow

A detailed study of the device angle dependency of a single vortex generator (VG) is presented in this chapter. A single Vortex Generator on a test section wall case, with four different device angles to the incoming flow, has been designed and solved by computational methods. The computational fluid dynamic (CFD) simulations have been compared with a wind tunnel experiment, where the corresponding parametric study was performed over a single vane mounted on the test section wall in a low-speed wind tunnel. In this experiment the flow was recorded using Stereoscopic Particle Image Velocimetry (S-PIV) in cross-planes at various positions downstream of the vane. The main objective is to study the angle dependency of a single VG mounted on a test section wall; for this purpose CFD simulations have been carried out and compared with wind tunnel experimental results and an analytical model both described in *Chapter 5*.

7.1 Introduction

CFD simulations have been carried out using the EllipSys3D CFD Code, Michelsen [34] and Sørensen [35], and compared with a wind tunnel experiment, where a parametric study were performed over a single vane mounted on the test section wall in low-speed wind tunnel. In this experiment the flow was recorded using Stereoscopic Particle Image

Velocimetry in cross-planes at various positions downstream of the vane. The experimental conditions and setup are the same as those described in Velte *et al.* [36] (see *Section 5.2*). In order to qualitatively compare the model with the measurement, the analytical VG model introduced in the thesis work of Velte [3] and described in *Section 5.3* is used. Based on the results of *Chapter 6*, the mesh-resolved VG model will be used for the simulations of this parametric study.

The main objective is to study the angle dependency of a single VG mounted on a flat plate. For this purpose CFD simulations have been carried out. So, the proposal of this research has been divided as Figure 7.1. shows.

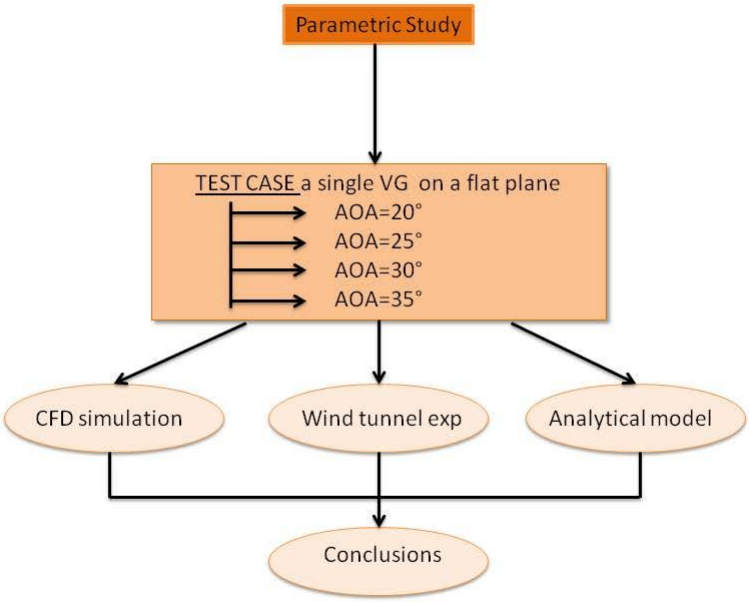

FIGURE 7.1: Study lay-out.

In all cases (CFD simulations, wind tunnel experiments and analytical model) the measurements have been conducted in a spanwise plane, normal to the test section floor, positioned five VG heights downstream of the vortex generator trailing edge, see Figure 7.2.

7.2 Computational Configuration

Steady state computations have been carried out and are compared to the experimental observations. These CFD computations were performed using the Ellip-Sys3D code, Michelsen [34] and Sørensen [35], as described in [40]. This in house CFD code is

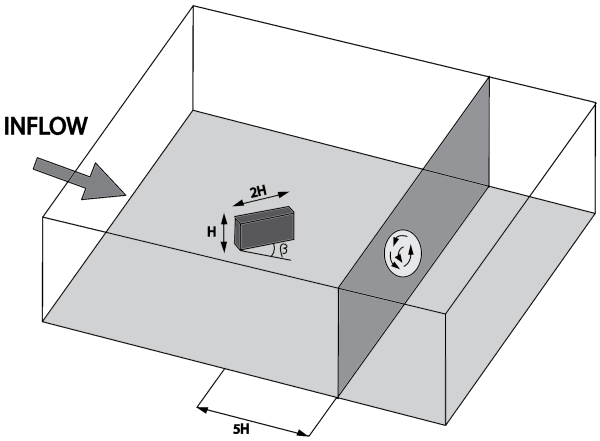

FIGURE 7.2: Plane location where the measurements were conducted.

a structured finite-volume flow solver using, in this work, Reynolds-Averaged Navier-Stokes equations. The pressure/velocity coupling is ensured using the SIMPLE algoritm and only steady-state computations have been performed. The convective terms are discretized utilising the third order Quadratic Upstream Interpolation for Convective Kinematics (QUICK), Khosla *et al.* [49]. For these computations the k-ω *SST* (Shear Stress Transport) turbulence model by Menter [50] was used. This case consists in a single VG on a flat plate and the computational domain has been defined with the following dimensions, normalized with the VG height, Figure 7.3. The flow domain width is 32 times the VG height and the height is 10 times. The flow domain length is 30 times the VG height in order to capture the generated vortex.

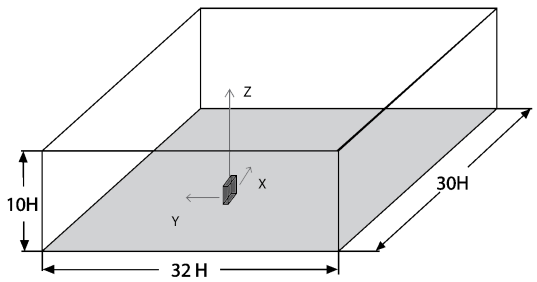

FIGURE 7.3: Computational domain of the CFD case.

The rectangular VG has an aspect ratio of 2:1, i.e., twice as long as its height, see Figure 7.4(a). The thickness of the vane is constant and with no sharp edges. A boundary layer is developed over test section floor, forced by the viscous interaction between the wall

and the flow. The VG was positioned test section floor in such way that the boundary layer thickness at this location is equal to the VG height.

(a) VG dimensions (b) VG angle

FIGURE 7.4: VG geometry.

The angle of attack defined is β degrees and four different angles have been selected for the parametric study: $\beta = 20°, 25°, 30°$ and $35°$, Figure 7.4(b). These angles were reached by the rotation of the mesh.

The Reynolds Number based on VG height H is Re=1700. The computational setup of the CFD simulations consists in a block structured mesh of 18 million cells with the first cell height (Δz/H) of 1.5×10^{-6} normalized by the VG height. Around the VG geometry, the mesh has 5×10^{6} cells, while the mesh downstream the VG for capturing the wake has approximately 2.5×10^{6} cells, see Figure 7.5. In order to resolve the boundary layer, cell clustering has been used close to the wall and the dimensionless distance from the wall of the first layer of cells is less than 2 ($y^{+} < 2$), as the *SST* turbulence model requires. Verification of the mesh was performed by a mesh dependency study. Results obtained for the finer mesh (66 blocks of 653 cells) are compared with results obtained for a standard (66 blocks of 333 cells) and a coarser mesh (66 blocks of 173 cells). A mesh dependency of around 5% has been detected on the axial velocity.

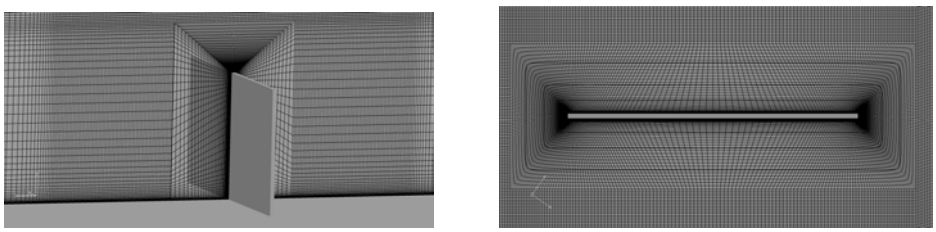

(a) Cross flow section (b) Horizontal section

FIGURE 7.5: Mesh around the vortex generator.

7.3 Results

Four different angles of attack β ($20°, 25°, 30°$ and $35°$) of the VG to the oncoming flow were chosen for the computations and subsequently, as a quantitative comparison, compared with the wind tunnel experiments and the analytical model described in Sections *Section 5.2* and *5.3*, respectively.

7.3.1 Computational Results

CFD results of a single VG on a flat plate were performed using the EllipSys CFD code. Figures 7.6(a), (b), (c) and (d) show the evolution of the vortex generated downstream the trailing edge of the VG for the CFD case with the device angle of incidence β as a ($20°, 25°, 30°$ and $35°$), respectively. The inner separation between planes is four times the VG height.

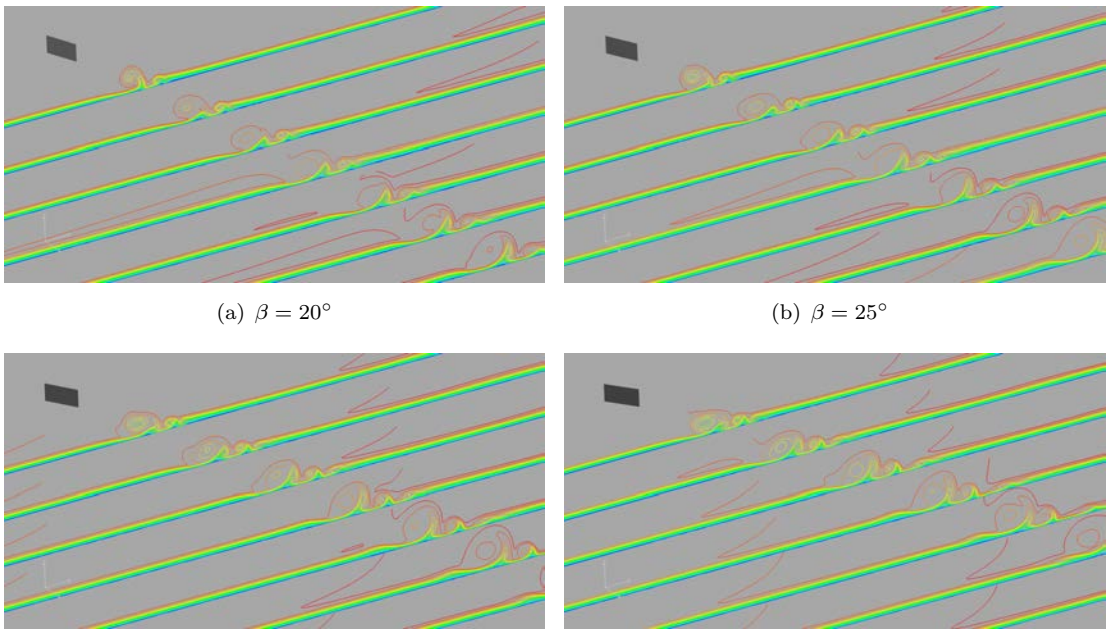

(a) $\beta = 20°$ (b) $\beta = 25°$

(c) $\beta = 30°$ (d) $\beta = 35°$

FIGURE 7.6: CFD results of vortex development downstream the VG with four different angles of attack.

Three parameters have been chosen for a qualitative comparison between the four different angles of β: axial velocity, axial vorticity and static pressure. Figure 7.7 illustrates the axial velocity and axial vorticity fields, respectively, and Figure 7.8 the pressure fields five device heights downstream the VG. In addition to this, a top view pressure field in a plane parallel to the wall up to 0.5 VG heights has been represented for each VG angle, see Figure 7.8 (right column).

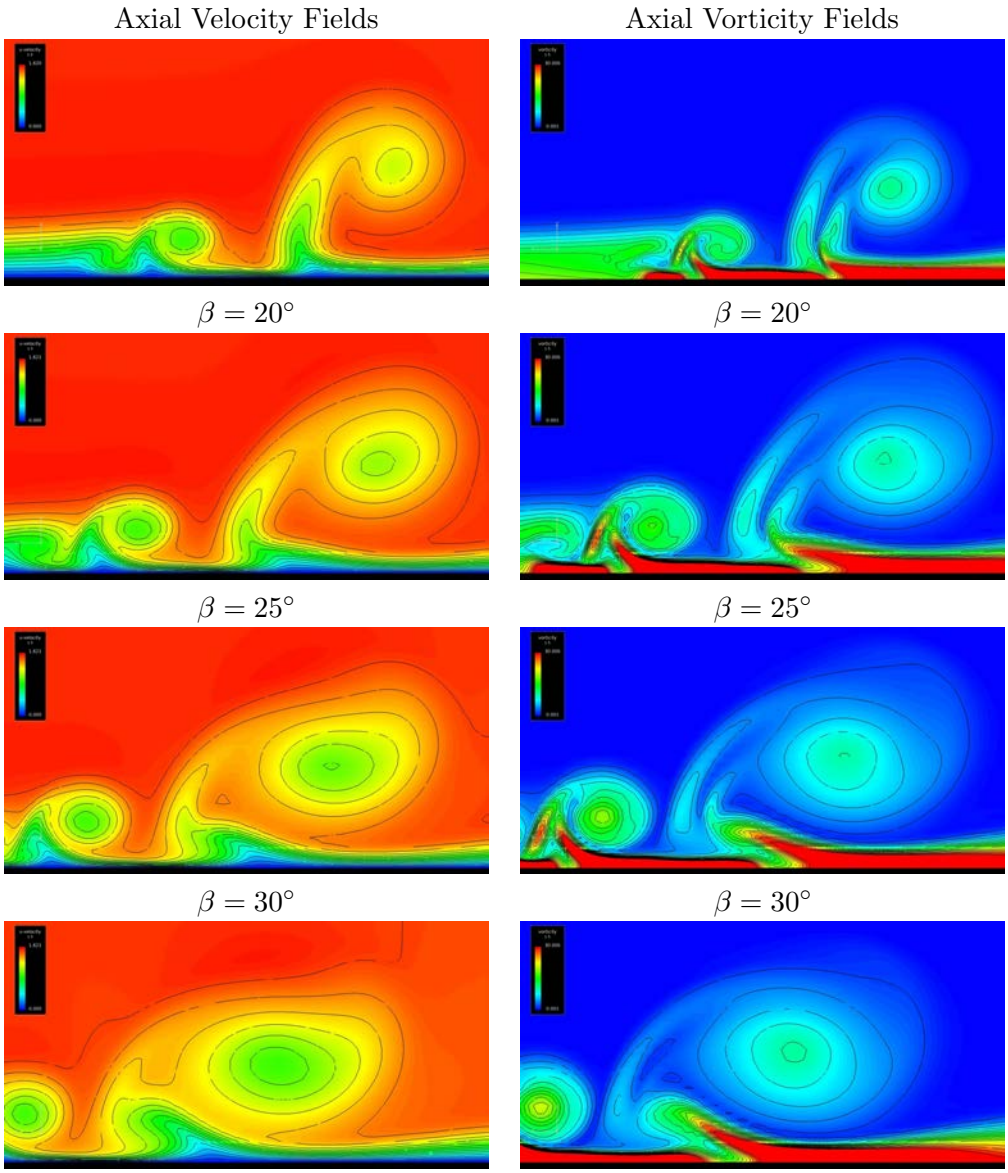

FIGURE 7.7: Axial velocity fields (left column) and vorticity fields (right column) at different angles of attack measured in a spanwise plane placed five device heights downstream the VG.

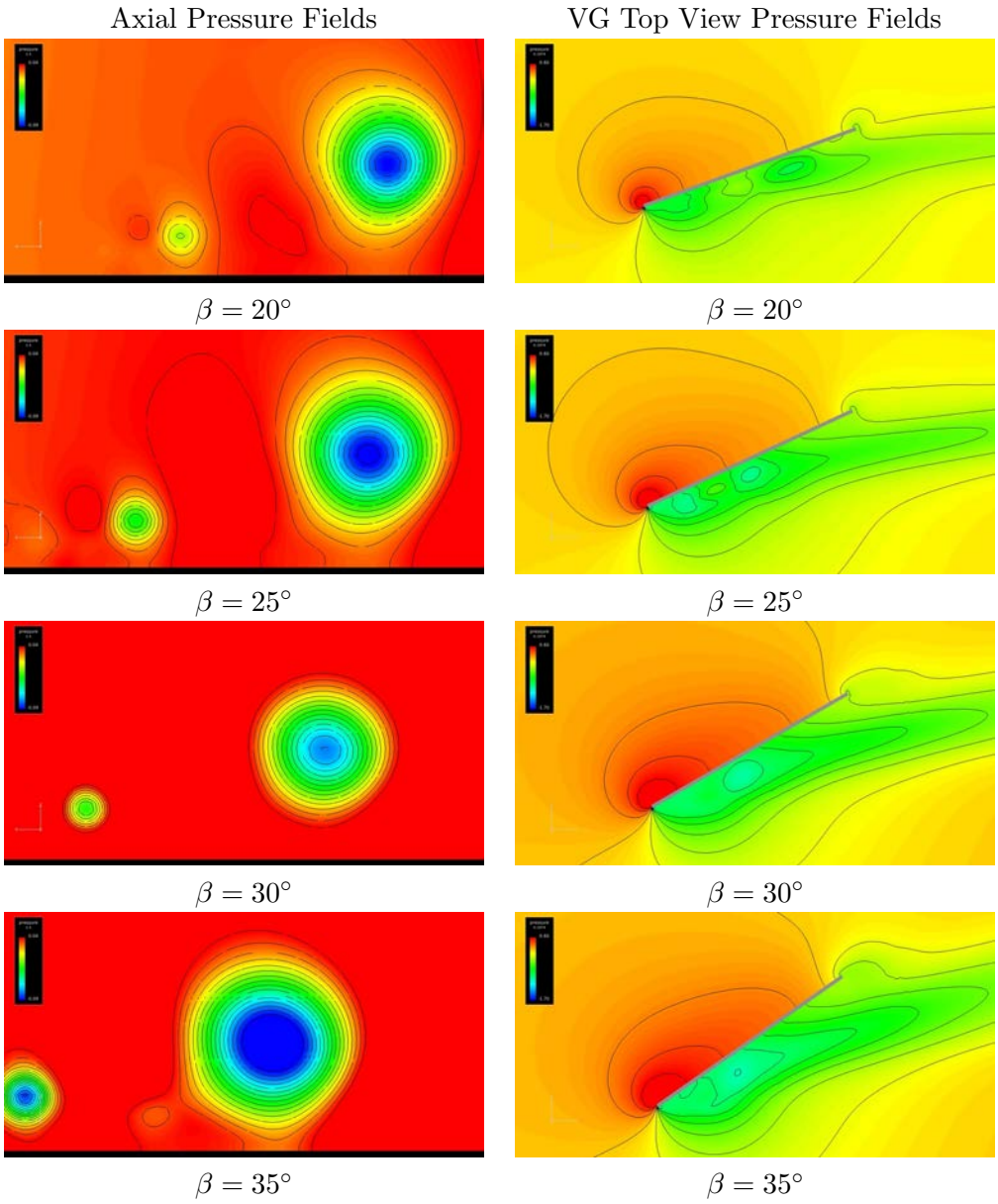

FIGURE 7.8: Axial pressure fields (left column) at different angles of attack measured in a spanwise plane placed five device heights downstream the VG. Top view pressure fields (right column) of the VG at different angles of attack.

7.3.2 Quantitative Comparison

As preciously mentioned, wind tunnel measurements and an analytical model of the primary vortex is considered in the context of the CFD simulations as a quantitative comparison. Figure 7.9 represents the axial u_z (upper) and azimuthal u_θ (lower) velocity profiles calculated for $20°, 25°, 30°$ and $35°$ degrees of the device angle. These values were extracted in a plane normal to the section wall five device heights downstream of the VG, along a line parallel to the wall passing through the centre of the primary vortex.

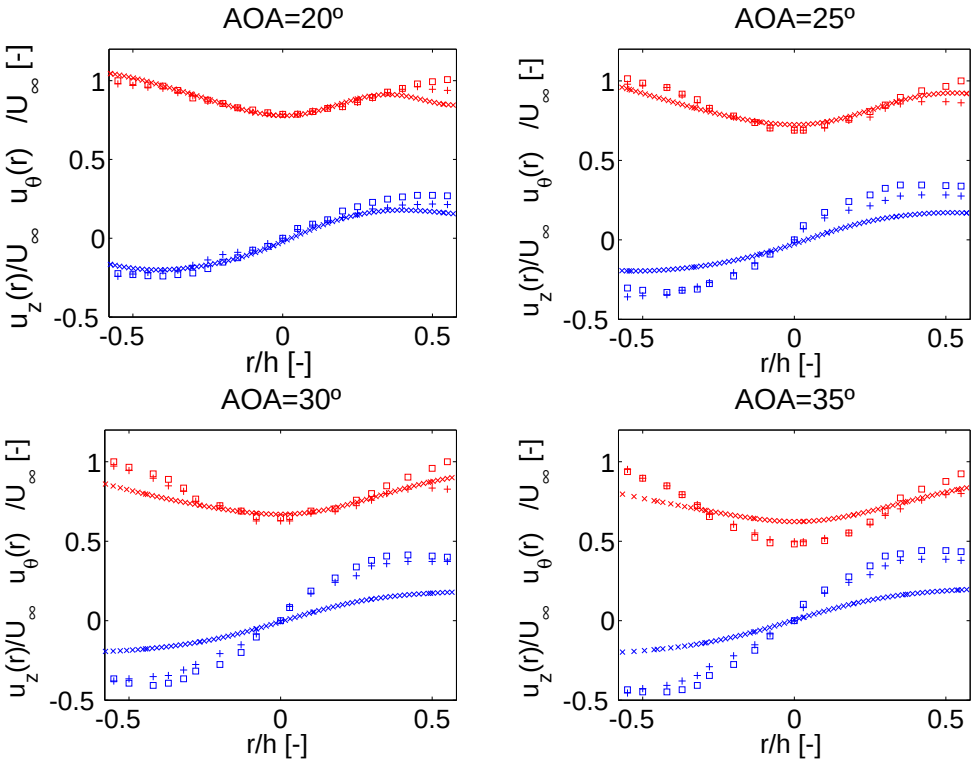

FIGURE 7.9: Comparison of axial and azimuthal velocities of embedded vortices generated by a vortex generator for four device angles β. (x) CFD results, (+) Wind tunnel experimental data, (□) Analytical Model. Upper values (red colour) are the axial velocity profile u_z and lower (Blue colour) the azimuthal velocity profile u_θ.

In order to analyse the quantitative differences between the computational results and the experimental data, the Root Mean Square Error RMSE has been calculated:

$$RMSE = \sqrt{\frac{\sum_{i=n}^{n}(a_{1,i} - a_{2,i})^2}{n}} \tag{7.1}$$

The differences between the wind tunnel measurements and the CFD computations are represented in Figure 7.10. Green colour bars illustrate the axial velocity differences and the yellow ones the azimuthal differences, both of them between the wind tunnel experimental data and numerical results of the CFD simulations.

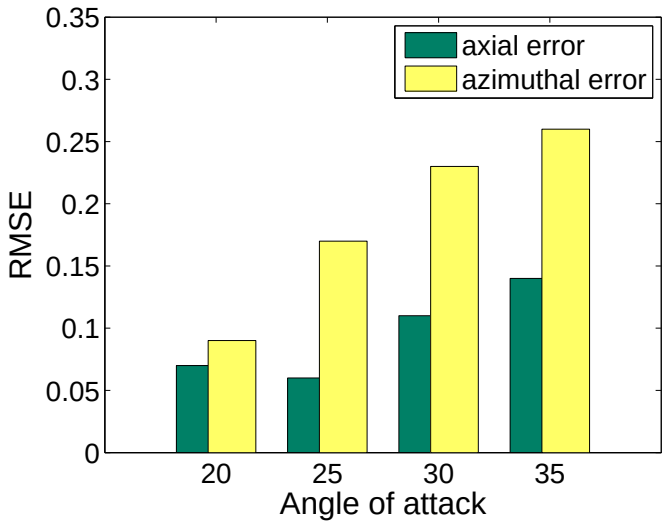

FIGURE 7.10: Root mean square error between the wind tunnel experimental data and CFD computations. Green colour bars represent the error in the axial velocity profiles and the yellow ones the azimuthal velocity profiles errors.

7.4 Discussion of the results

Simulations results of 20° and 25° degrees of the device angle compare well with the experimental and the analytical model. However, significant differences were observed as the angle of attack increases. One reason for these differences could be that the boundary layer evolution along the wall was not accurately performed in the simulations to reproduce the same boundary layer profile facing the leading edge of the VG as in the wind tunnel experiments. Further, the turbulence model is not designed to capture large scale motions such as the vortex, but rather turbulent fluctuations, which may explain why the results get increasingly worse with higher vane angles β. Further, the averaged simulations may not be able to accurately capture the mean field of this highly dynamical flow since the meandering of the vortex core affects the vortex core obtained in the average velocity field. As Figure 7.9 shows, at 20 degrees of angle of attack the CFD results are well matched with wind tunnel experimental data and the analytical model, both for the axial and azimuthal velocity profiles. Also, the advection velocity in both cases matches very well. However, the perturbation from a secondary vortex (see also Figures 7.7 and 7.8), which is observed in the asymmetry to the right in the axial velocity profiles, seems to be stronger in the CFD case. This secondary vortex is present with variable strength at all considered device angles, introducing a disturbance in the flow field of the main vortex. However, the influence is more notable in the case of 20 degrees. In the 25 degrees of angle of attack case, the axial velocity profiles show excellent agreement in all the cases, though the azimuthal velocity profile of the CFD case starts displaying relevant differences with the wind tunnel data and

the model. For all four VG angles it is seen that the axial velocity is predicted much better than the azimuthal one. In the azimuthal profiles, it is evident that the swirl increases with increased angle of attack. Unfortunately, the CFD simulations are not able to accurately capture this increase.The bar chart of Figure 7.10 illustrates that, when the device angle is increasing, the RMSE increases as well, above of all in the azimuthal velocity profiles. These differences in the azimuthal velocity profiles could be explained due to the difficulties of the turbulent models to capture the swirling flows with high accuracy.

7.5 Conclusions

Vortices generated by a passive rectangular vane-type vortex generator of the same height as the boundary layer thickness in a flat plate have been studied. CFD computational simulations with four different angles of attack β ($20°, 25°, 30°$ and $35°$) of the VG to the incoming flow have been carried out using the RANS method and compared with wind tunnel experimental data and an analytical model. Some differences have been noticed between the computational results and the experimental ones, foremost in the azimuthal velocity profiles. Further, it was observed that the differences in the axial and azimuthal velocity profiles produced by the simulations as compared to the experiments/analytical model grow as the device angle increases. More work is therefore required in order to address these problems. For future investigations, it would be highly interesting to achieve more experiments and CFD simulations at higher Reynolds numbers, which provide more realistic flow conditions for most applications. Actually, experiments have already been performed in a high Reynolds number boundary layer and are under processing. This boundary layer, produced in a unique wind tunnel in Lille, France, can accurately follow the well known log-law, which is implicitly assumed in turbulence models, and these measurements will therefore naturally form a better basis for CFD validation once the processing is finalized.

Part III

Testing of Self-similarity and Helical symmetry on Vortex Generator Flow Simulations

Chapter 8

Self-similarity and Helical Symmetry of a Rectangular Vortex Generator Wake in a negligible streamwise pressure gradient flow

According to experimental observations, the vortices generated by vortex generators have previously been observed to be self-similar for both the axial (u_z) and azimuthal (u_θ) velocities, see [4]. Furthermore, the measured vortices have been observed to obey the criteria for helical symmetry, see [36]. These are powerful results, since it reduces the highly complex 3D flow to merely four parameters. In this study, corresponding computer simulations using Reynolds-Averaged Navier-Stokes equations have been carried out and compared to the experimental observations. The main objective of this study is to investigate how well these simulations can reproduce these aspects of the physics of the flow, i.e., investigate if the same analytical model can be applied. This is especially interesting since these types of flows are notoriously difficult for the turbulence models to predict correctly. Using this model, parametric studies can be significantly reduced and, moreover, reliable simulations can substantially reduce the costs of the parametric studies themselves.

8.1 Introduction

Many models for the generated vortices have been presented over the years. Theoretical models include, for example, the one by Smith [51] and a model presented by Velte *et al.* [36] that was developed and applied to show the helical symmetry of the vortices generated by a passive rectangular vane-type vortex generator. As for models incorporated into codes that rather describe the numerical implementation of VGs than the flow physics, most are variants of the practical BAY-model by Bender *et al.* [22], which introduces body forces using source terms in the Navier-Stokes equations.

The fact that the vortices produced by vortex generators possess helical symmetry means, in effect, that the streamwise velocity profiles (u_z), along the longitudinal vortex axis and the rotational (u_θ) flows are inter-related by a simple linear relation based on the helical shape of the vorticity lines [36, 48]. Further, previous experimental work by Velte [4] examines the downstream vortex evolution behind a cascade of vortex generators producing counter-rotating vortices in a boundary layer of negligible streamwise pressure gradient. The model parameters are all seen to vary linearly in the downstream direction. Based on the experimental observations of a previous study [4], the vortices generated by vortex generators have been observed to be self-similar for both the axial (u_z) and azimuthal (u_θ) velocity profiles. The previous model, which is based merely on u_z and u_θ at one single downstream location, can therefore be extended to include the full downstream evolution of the developed part of the vortex using self-similarity scaling arguments. This knowledge is important for fundamental understanding as well as for the aspect of applications, for which parametric experiments can be substantially reduced in terms of required time and cost.

Self-similarity is a state of self-preservation across scales. For jets and wakes this classically means that the development of the streamwise velocity profiles in the streamwise direction collapse for all positions if scaled correctly according to the theory presented, e.g., by White [33]. Figure 8.1(a) illustrates the wake velocity profile of a single VG on a flat plate at a distance d from the trailing edge of the vane, where U_∞ is the free stream velocity and u_0 the convection velocity (Δu and ε represent the characteristic velocity scale and the characteristic shear-layer width, respectively). A sketch of the axial velocity profiles development of the wake downstream of a VG is shown in Figure 8.1(b).

In the present study CFD simulations have been carried out by EllipSys3D CFD Code (Michelsen [34] and Sørensen [35]), and compared with a wind tunnel experiment together with the analytical model (both described in *Chapter 5*), using a test case of a

single vane mounted on the test section wall in a low-speed wind tunnel. The main objective of this work is to investigate how well the simulations can reproduce the physics of the flow and if the same analytical model can be applied. The use of this model can be a reliable tool to decrease the cost of the parametric studies of vortex generator flow simulations.

Using this model, parametric studies can be significantly reduced and, furthermore, reliable simulations can substantially reduce the costs of the parametric studies themselves.

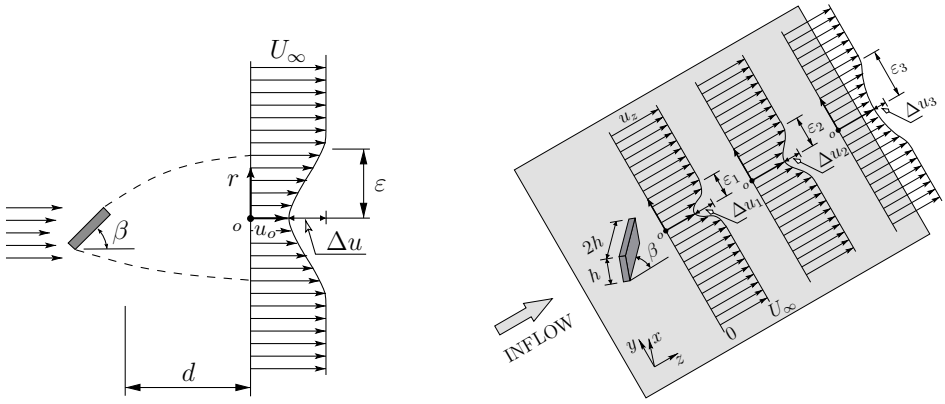

(a) Wake of a single vortex generator at a distance d.

(b) Wake development illustrated by streamwise velocity profiles.

FIGURE 8.1: Wake velocity profiles of a single vortex generator.

8.2 Computational configuration

In this study, steady state simulations were carried out and compared to the previous experimental observations. These computations were performed using the EllipSys3D code, see Michelsen [34] and Sørensen [35]. This in-house CFD code is a structured finite-volume flow solver using, in this work, Reynolds-Averaged Navier-Stokes equations. The pressure/velocity coupling is ensured using the SIMPLE algorithm. The convective terms are discretized utilising the third order Quadratic Upstream Interpolation for Convective Kinematics (QUICK), [49]. For these computations the $k-\omega$ *SST* (Shear Stress Transport) turbulence model by Menter [50] was used.

Figure 8.2 illustrates the computational setup with the current setting consisting of a single VG on a flat plate. The computational domain with dimensions normalized with the VG height are also given in Figure 8.2, as also described in [40]. The thickness of the vane is constant and the VG was positioned directly on the wall at a position where the boundary layer thickness is equal to the VG height.

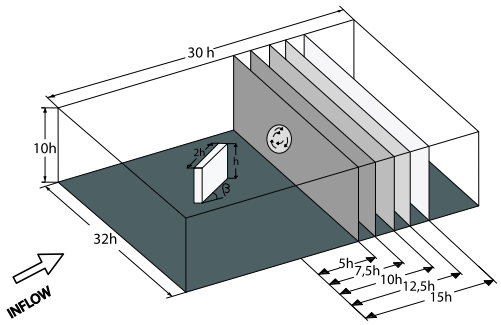

FIGURE 8.2: Computational domain

The VG angle of attack to the oncoming flow is β=20^o and the Reynolds number based on VG height h=0.25 m is Re = 1700, using an inflow velocity U_∞= 1 ms^{-1} and a fluid density of 1 kg m^{-3}. The computational setup of the CFD simulations consists of a block structured mesh of 18 million cells with the first cell height (Δz/h) of 1.5×10^{-6} normalized by the VG height. In the immediate vicinity of the vane, the mesh has 5×10^6 cells, while the mesh downstream the VG for capturing the wake has approximately 2.5×10^6 cells. In order to resolve the boundary layer, cell clustering has been used close to the wall and the dimensionless distance from the wall of the first layer of cells is less than 2 ($y^+ < 2$), as is required by the SST turbulence model.

Verification of sufficient mesh resolution was performed by a mesh dependency study. Results obtained for the finer mesh (66 blocks of 64^3 cells) are compared with results obtained for a standard (66 blocks of 32^3 cells) and a coarser mesh (66 blocks of 16^3 cells). The deviation between the coarsest and the finest mesh indicates a difference of $\sim$5% in the axial velocity. The simulations were converged until a satisfactory residual convergence was achieved on the velocities, pressure and turbulence variables.

In the computational simulations, data were extracted in 5 spanwise planes, normal to the test section floor and the oncoming bulk flow. Those planes were located 5, 7.5, 10, 12.5 and 15 VG heights downstream of the vortex generator trailing edge, as sketched in Figure 8.2.

8.3 Results

The analysis of helical symmetry was performed on computational results extracted in the cross planes positioned at z/h = 5, 7.5, 10, 12.5 and 15 VG heights downstream of the trailing edge of the VG. An angle of attack of β=20^o of the VG to the oncoming flow was chosen for the computations and subsequently compared with the wind tunnel

experiments and the analytical model described in sections *Section 5.2* and *Section 5.3*, respectively. The vane angle is close to the optimum found by Godard and Stanislas [20] in a parametric study optimizing separation control. The extraction of velocities from the computations was conducted in a similar way to the experimental procedure described in [36], in planes normal to the section wall downstream of the VG and applying polar coordinates (r, θ) to the vortex with the origin at the vortex center.

8.3.1 Testing of helical symmetry

The solid curves in Figure 8.3.1 illustrate the axial and azimuthal velocity profiles (upper curves are the axial velocity profile u_z and lower the azimuthal one u_θ) for each plane position where the data is extracted along a horizontal line through the vortex center. These curves are compared to what is obtained from the right-hand side of (5.7b) described in *Section 5.3*, finding l by least squares fitting of the residual, (o). The two data sets overlap well for all plane positions, confirming that the computational results fulfill the criterion for helical symmetry just like the experimental ones do. Note that the analysis has been carried out only on the right side in the figures, due to a perturbing secondary vortex appearing on the left side yielding an asymmetric velocity profile [36].

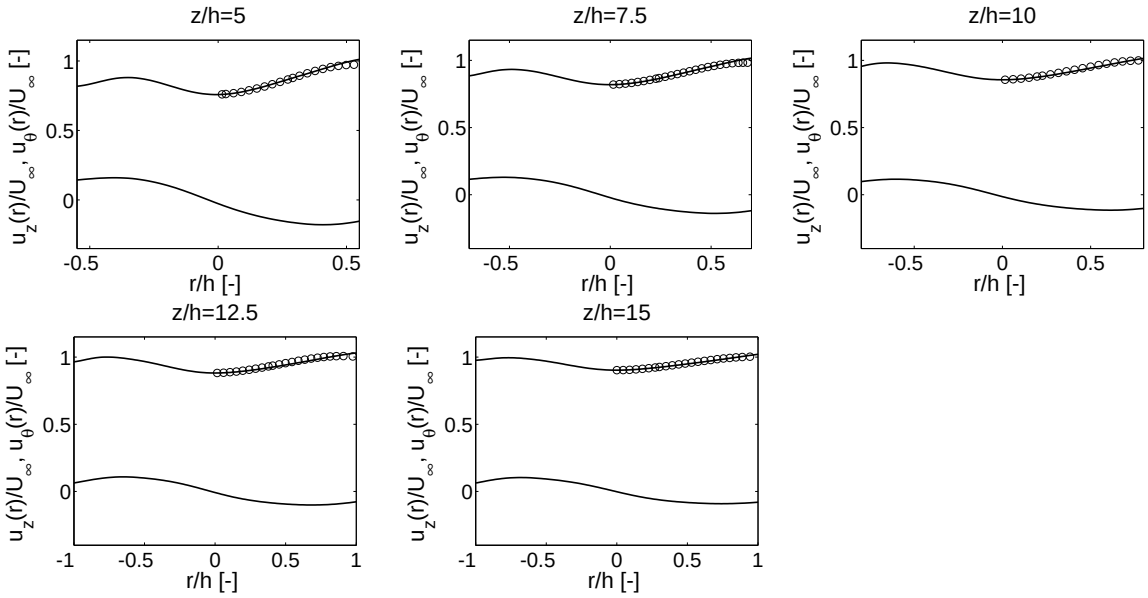

FIGURE 8.3: CFD velocity profiles of embedded vortices generated by a VG for a device angle $\beta = 20^o$. Upper values are the axial velocity profile u_z and lower the azimuthal one u_θ normalized by U_∞. CFD values of u_z are compared to the right-hand side of (5.7b) calculated using the computational values u_θ (o).

8.3.2 Testing of wake self-similarity

The three velocity components were extracted diametrically along lines passing through the center of the primary vortex at four angles of Θ (0^o, 45^o, 90^o and 135^o) to cover the full rotational variations of the vortex, see Figure 8.4.

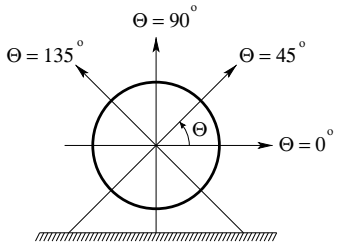

FIGURE 8.4: Polar coordinate system applied to the vortex.

Figures 8.5 and 8.6 display the axial (u_z) and azimuthal (u_θ) velocity profiles of the measurements and computational data, respectively. The left column shows a combined plot of the axial and azimuthal velocity profiles for all downstream positions. The mid and right columns show the self-similarity scaled axial and azimuthal velocity profiles, respectively. Note that these profiles all collapse nicely. Note also that in the left side of these profiles, in particular for the axial velocity, the perturbations caused by the secondary vortex appear.

From visual inspection of the left column in Figure 8.5, it becomes apparent that the axial and azimuthal velocity profiles in the vortex core do not change significantly for the various extraction angles θ. Of course, the presence of the wall and the emergence of the perturbing secondary structure create distortions in the outer regions of the core, which is particularly observable on the left side of the plots for $\theta = 45°$, $90°$ and $135°$. Similar qualitative observations can be done for the computational results in Figure 8.6, though some features are pronounced to greater or lesser extent; The effects of the secondary perturbing vortex is more clearly visible in the axial velocity profiles for $\theta = 0°$ and the speed-up in the azimuthal velocity close to the wall is much greater for $\theta = 90°$ compared to the measurement results. Both of these discrepancies can be attributed to the vortex core strength being larger (which will be observed later in Figures 8.7 and 8.8) and the vortex core distance to the wall being smaller in the computations. The last effect can also be attributed to the vortex core size being larger in the simulations, see Figures 8.7 and 8.8. A stronger primary vortex positioned closer to the wall will naturally cause stronger swirl velocities and a larger spanwise adverse pressure gradient at the wall, causing the separation (i.e., secondary vortex core) to increase in strength, hence increasing the perturbations on the primary vortex. Further, some general differences between the measured and the computed velocity profiles are observed; The axial velocity induction is not as pronounced in the computations as in

the measurements. This is apparent from the smaller deficit in the wake profiles of the computations in the left column of Figure 8.6 as compared to the measured ones in Figure 8.5. The swirl velocities are also generally observed to be smaller in the computed flow. Secondly, the vortex core size (distance between the extreme swirl velocities in the right column of Figure 8.6) varies more than in the measurements. The vortex core is also larger in the computations than in the measurements, as can be seen by comparing the left columns of Figures 8.5 and 8.6.

Figures 8.7 and 8.8 display the stream-wise evolution of the helical parameters: vortex convection velocity (u_0), circulation (Γ), helical pitch (l) and vortex core radius (ε) for the wind tunnel experiments and computational simulations, respectively. The local flow characteristic u_0 was found directly from the lowest value of the axial velocity wake profile in the vortex core and the helical pitch l was obtained from least-squares fitting of (5.7b). The circulation has been calculated as the flux of vorticity across a surface enclosed by a curve described by the vortex radius. The vortex core radius ε has been obtained as the radius of the maximum value of the azimuthal velocity for each plane position. For a better comparison between the experimental and computational results, both vortex radius and helical pitch have been normalized by the VG height h and averaged across the azimuthal coordinate θ. The convection velocity has been normalized by the free stream-velocity U_∞ and the circulation by the product $U_\infty\ h$. Since the axial and azimuthal velocities are observed to be self-similar, it is expected that u_0 and l also vary linearly along the downstream path, which is indeed observed for both the experiments and the simulations in Figures 8.7 and 8.8. As expected, the only factor which does not vary along the plane positions is the circulation, which should naturally be close to constant in a system of low viscous dissipation.

In fact, all helical parameters are seen to vary linearly with the downstream distance, both for experiments and simulations. Further, the general trends agree in the downstream evolution of all parameters, though the absolute values differ between the quantities. As pointed out earlier, the vortex strength is larger in the simulations and the vortex core size is also somewhat larger and varies with a steeper gradient in the downstream direction. The convection velocity (minimum axial velocity at the center of the vortex core) was also observed to be smaller in the measurements, which is again confirmed in Figures 8.7 and 8.8. Due to the helical symmetry of the vorticity lines, this means that the induction caused by the helical vorticity lines is stronger in the measurements than in the simulations. The relation between the convection velocity and the helical pitch is not as straightforward though, since the strength of the vorticity lines may vary. The variations in helical pitch and vortex core radius for different angles θ are spread quite similarly between the measurements and the simulations, though the gradients in the downstream direction vary somewhat.

Though the simulations are not perfectly able to mimic the measured flow, the general trends in the flow are captured and the simulations are able to reproduce both the helical symmetry (linear relation between the axial and azimuthal flow) as well as the self-similar behavior in the mean velocity profiles.

8.4 Discussion of results

In general, the simulations are able to reproduce the physics of the flow downstream of the VG. The helical symmetry of the main vortex generated by a rectangular VG in a negligible streamwise pressure gradient flow has been tested and compared with the analytical model developed in [36] with good agreement. Self-similarity behavior has also been confirmed in several positions downstream of the VG. Furthermore, four characteristic vortex parameters have been analyzed: convection velocity, circulation, helical pitch and vortex core radius. The trends of these parameters of the computational simulations are in line with the ones observed from the experiments. However, some discrepancies are visible in the values of these parameters. The computations under predict the values of the convection velocity, while the helical pitch and the vortex radius are over predicted. These discrepancies could be explained by the assumption of isotropy of the eddy viscosity models, causing problems in predicting the behavior of rotating flows. Further, the temporal behavior of the inlet conditions used in the simulations could not be captured in the experiments. The turbulence models are designed to simulate turbulent variations in the flow, and therefore may have troubles simulating the large-scale flow variations of the primary as well as the secondary vortices.

8.5 Conclusions

Vortices generated by a passive rectangular vane-type vortex generator of the same height as the boundary layer thickness above a test section wall have been studied. CFD simulations at Reynolds number Re=1700 have been carried out using the RANS method and compared with wind tunnel experimental data and an analytical model.

The vortex generated by the VG shows self-similar behaviour for both the axial and azimuthal velocity profiles. It was proven based on data from five plane positions $z/h = 5$, 7.5, 10, 12.5, 15 downstream of the trailing edge of the VG and with the angle of attack β=20^o of the vane to the oncoming flow. The CFD results in Figure 8.6 show relatively good agreement with the self-similarity shown in the experiments carried out in [4] and the trends of the characteristic helical vortex parameters in the computational

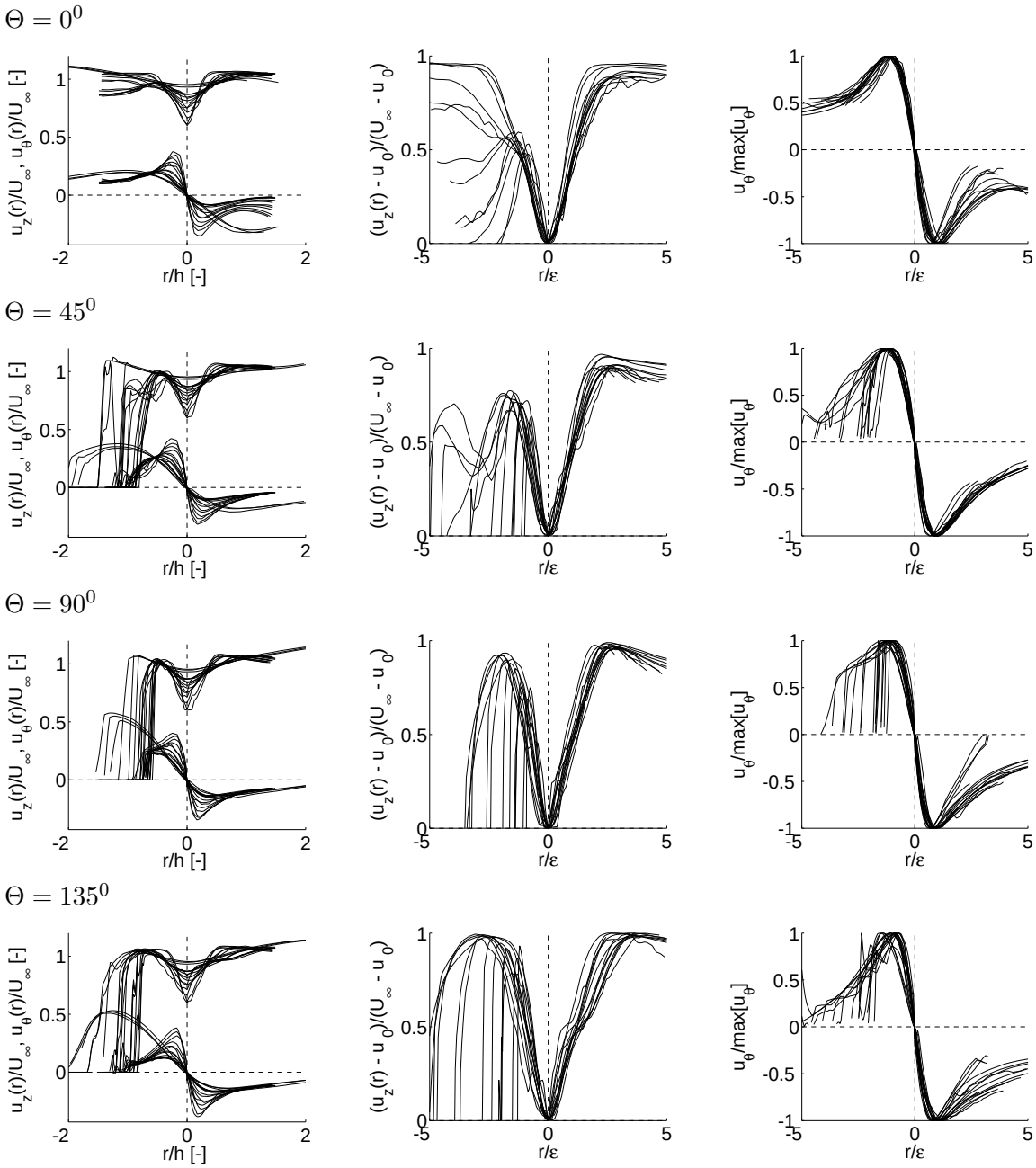

FIGURE 8.5: Velocity profiles from wind tunnel experiments for various angles Θ and z/h = 2-13, showing the experimental values of the axial (u_z) and azimuthal (u_θ) profiles (left column) and the axial (middle column) and azimuthal (right column), scaled by self-similarity variables (results from [4]).

results (Figure 8.8) match the experimental observations reasonably well (Figure 8.7) considering the limitations of the turbulence models and the applied inlet conditions.

From the point of view of self-similarity, computational simulations are able to reproduce the physic of the vortex generated by a rectangular VG with considerable reliability. Also, the helical symmetry has been tested and verified based on the computational data.

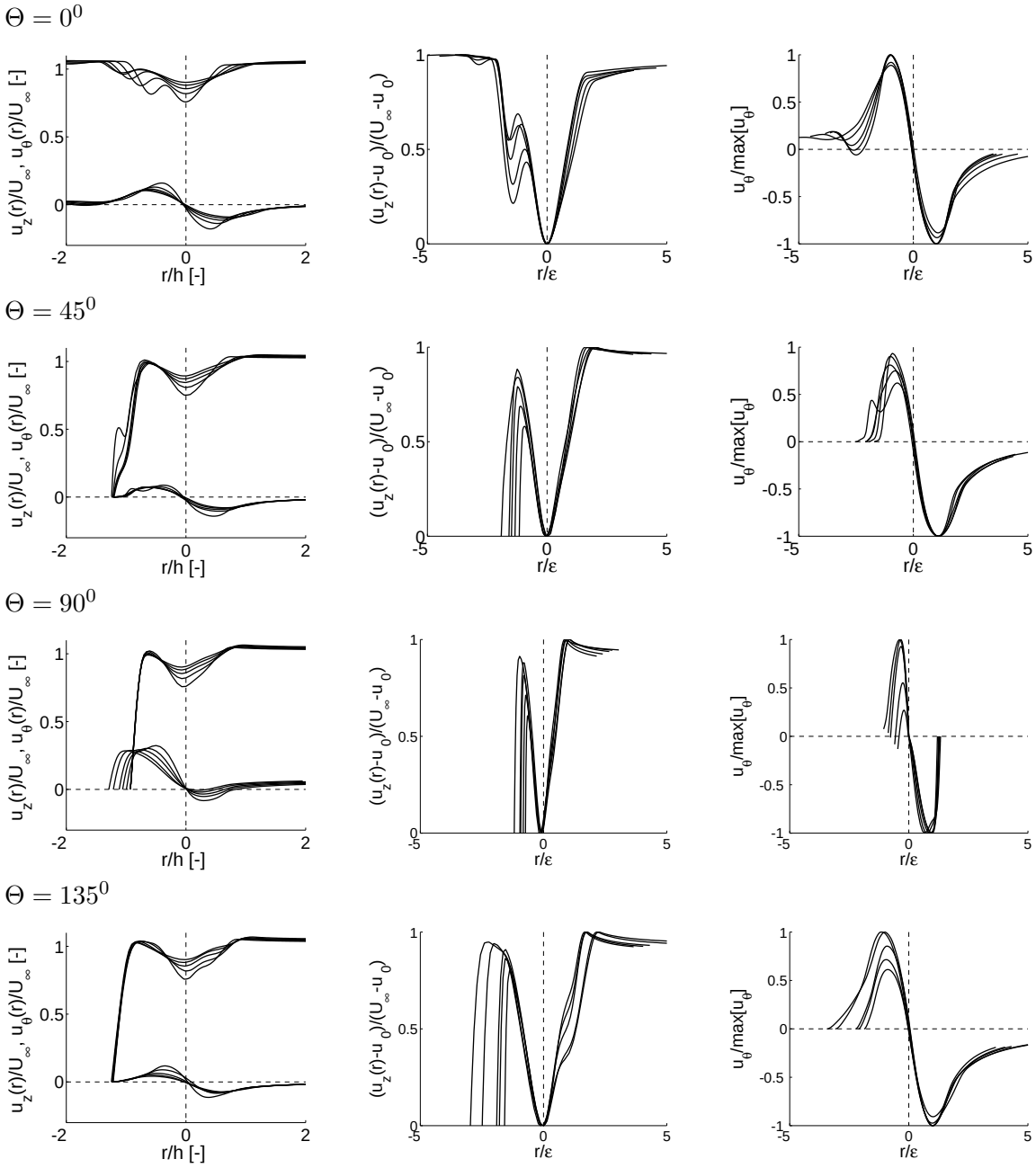

FIGURE 8.6: CFD velocity profiles for various angles Θ at five plane positions z/h = 5-15. The left side shows the axial (u_z) and azimuthal (u_θ) profiles and the middle and right sides show the axial and azimuthal profiles respectively, scaled by self-similarity variables.

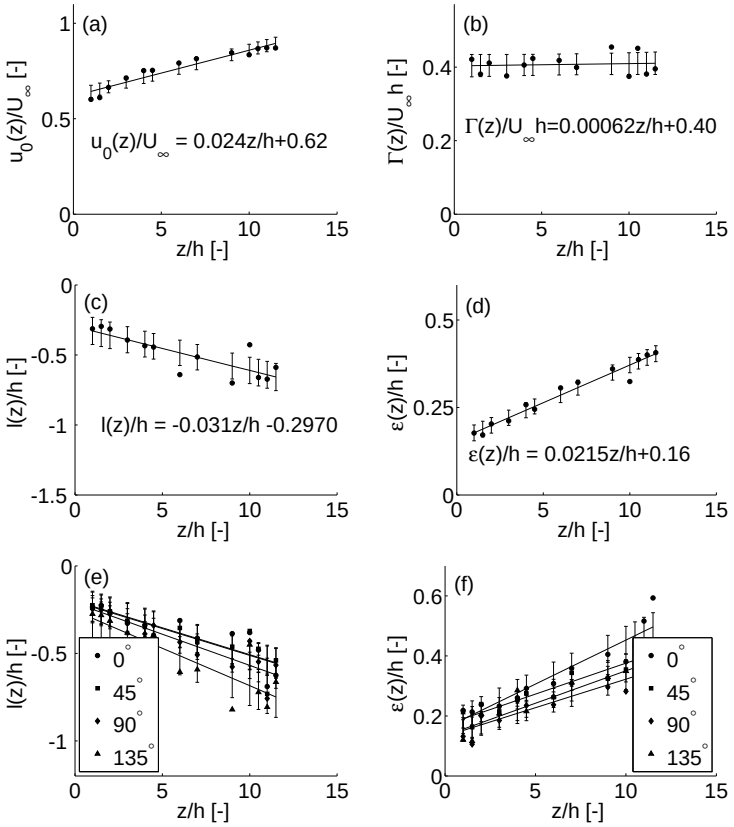

FIGURE 8.7: Experimental results of the downstream evolution of the characteristic vortex parameters in the stable wake (results from [4]).

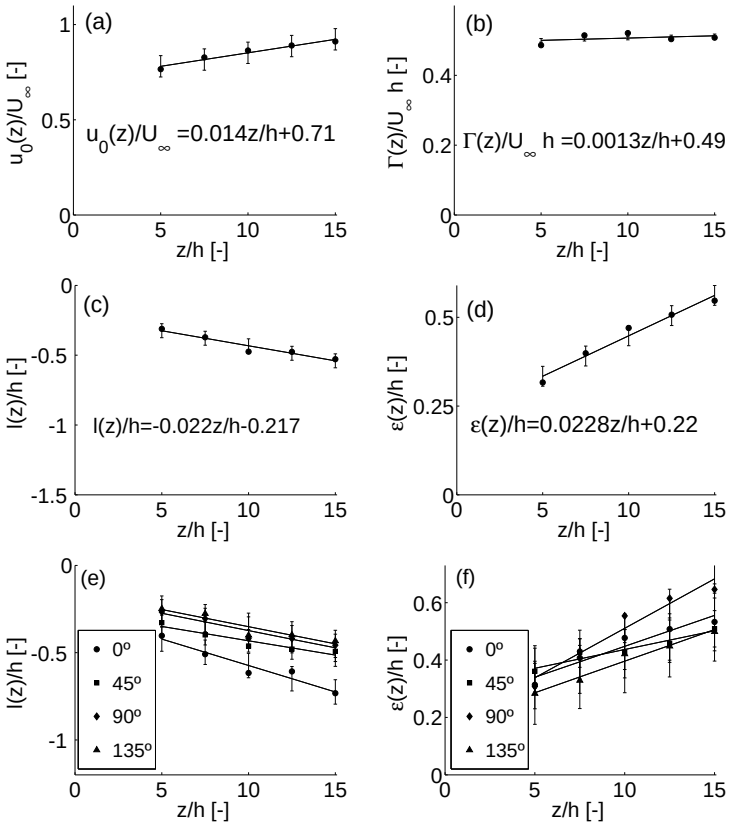

FIGURE 8.8: CFD results of the downstream evolution of the characteristic vortex parameters.

Part IV

Self-similarity and Wake Equilibrium Analysis on Two-dimensional Turbulent Wakes

Chapter 9

Wake equilibrium parameters of twin-plate simulations

Turbulent free shear flow of drag-producing obstacles has been extensively investigated. The free turbulent mixing procedure is an inevitable and vital process in numerous realistic phenomena of aerodynamics, see e.g. Townsend [24], Harsha [25] and Patel *et al.* [26]. Prabhu et al [27] and Narasimha *et al.* [28] conducted some experiments on plane turbulent wakes undergoing transition from an initial equilibrium state to a different final one. These experiments showed evidence of self-similar behaviour of the wake behind different wake generators. Later, Hebbar [29] and Wygnanski *et al.* [30] investigated the boundary layers and wakes of various wake generators where detailed measurements of two-dimensional profiles of static pressure, mean velocity, turbulence intensity and Reynolds shear stress were analyzed. Fernández-Gámiz *et al.* [31] and Velte [4] also investigated numerical and experimentally the self-similar manners of the wake on a rectangular vortex generator on a flat plate.

A flow is said to be self-preserving if solutions to its dynamical equations and boundary conditions exist for which, throughout the evolution of the wake, all dynamical parameters have the same relative value at the same relative position, George [32]. These parameters are sketched in Figure 9.1, where U_∞ is the free stream velocity, u_0 the convection velocity and W_0 and δ the defect velocity and the half-defect thickness, respectively. Therefore, according to Narasimha *et al.* [28], an equilibrium wake state is defined as one in which the mean velocity and the turbulent stresses exhibit similarity with identical length and velocity scales.

In this work, a detailed numerical analysis of two dimensional mean velocity profiles downstream of two parallel flat plates was carried out at a Reynolds number of 3.2×10^4 (based on the plate length L and free stream velocity $U_\infty = 1\, ms^{-1}$) using Reynolds

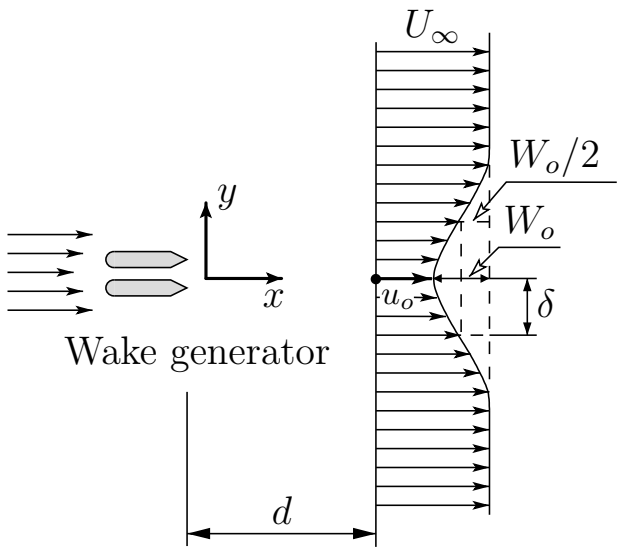

FIGURE 9.1: Sketch showing the main wake parameters behind a twin-plate

Averaged Navier-Stokes (RANS) simulations and have been compared with experimental data. Furthermore, a self-similar study of the wake behind the twin plate was carried out based on the computer simulations. The purpose of this work is to study the manner in which the results of computational simulations of a twin-plate (see Figure 9.1) at moderate Reynolds numbers approach the self-preserving state described in Sreenivasan *et al.* [37].

9.1 Governing equations of the plane wake

According to Townsend [24] the governing equation for a 2D wakes in a uniform stream to first order is:

$$U_\infty \frac{\partial}{\partial x}(u - U_\infty) = -\frac{\partial}{\partial y}\overline{uv} \tag{9.1}$$

where U_∞ is the free stream velocity outside of the wake. Momentum integration yields:

$$\int_{-\infty}^{+\infty} U_\infty(u - U_\infty)dy = U_\infty^2\,\theta = \frac{M}{l} \tag{9.2}$$

where θ is the momentum thickness of the wake velocity profile and M the momentum defect per unit length on the wake generator.

A plane turbulent wake is considered as a deficit in a moving stream. It has a much stronger effect due to the convective acceleration than a jet. So, in that case, self-similarity is achieved if:

$$\frac{W}{W_0} = \text{fcn}\left[\frac{y}{b(x)}\right] \tag{9.3}$$

where W and W_0 are defined as wake defect velocity and center line wake defect velocity, respectively. y is the distance normal to the mean flow starting in the center line of the wake and $b(x)$ represent the shear layer width in the corresponding plane position. The average pressure in the free wake is nearly constant (except for turbulent fluctuations effects) due to an open environment. This time, the momentum theorem states that the drag force F related to the wake profile is independent of x:

$$F = \int_{-\infty}^{+\infty} \rho\, u\, W_0\, dA = const \approx (const)\, \rho\, U_\infty\, W_0\, b \tag{9.4}$$

Thus, in the case of plane wakes, W_0 is proportional to b^{-1}. A uniform free stream velocity outside the wake and a small-defect $w \ll U_\infty$ are assumed. When these facts are substituted in the boundary layer equations with the small-defect assumption $u(\partial u/\partial x) \approx U(\partial u/\partial x)$, similarity state is achieved if:

$$b = const \cdot x^{\frac{1}{2}} \qquad W_o = const \cdot x^{-\frac{1}{2}} \tag{9.5}$$

The constants in equation (9.5) that determinate the variation of w_0 must be found through experiments. Sometimes it is difficult because due to the large-scale structures, e.g., Karman vortex streets, similarity is not reached until hundreds of diameters downstream of the body, Wygnansky *et al.* [30].

According to the analysis of turbulent wakes made in [32] the wake can be considered in the far field to be generated by a point called "point of drag", which is totally characterized by the kinematic drag $U_\infty^2\theta$ and the distance x downstream from the trailing edge. Thus, on dimensional grounds,

$$W_0 = W_0(x, U_\infty^2\theta) \quad \Rightarrow \quad \delta = \delta(x, U_\infty^2\theta) \tag{9.6}$$

related to the momentum integral constraint

$$W_0\,\delta \sim U_\infty \theta \tag{9.7}$$

From equations (9.6) one can write

$$W_0 \sim U_\infty \left(\frac{\bar{\theta}}{x}\right)^{\frac{1}{2}} \qquad \delta \sim (x\,\bar{\theta})^{\frac{1}{2}} \tag{9.8}$$

9.2 Experimental data

The experimental setup is the one of Sreenivasan *et al.* [37]. The experiments were conducted in an open circuit suction type wind tunnel with a Reynolds number $Re = 3.2 \times 10^4$ based on the twin plate length L (see Figure 9.2) and a free stream velocity $U_\infty = 21.3ms^{-1}$. The free stream turbulence level at this velocity was measured about 15%. The wind tunnel test section was 30 × 30 cm in cross section and 4.27 m long with a contraction ratio of about 10 : 1. Less than 1.5% of variation in the wind speed along the test section was obtained by applying suitable divergence for the boundary layer growth. All mean velocity measurements were made with a pitot-static tube and hot-wire measurements with suitable frequency compensation showed that the maximun value of u'/U_∞ (u' is the root-mean-square streamwise velocity fluctuation) ranged from about 4% in the near wake and to about 1.6% at the far wake.

9.3 Computational Configuration

Two-dimensional steady state simulations were carried out (as described in [52]) and compared to the previous experimental observations. These computations were performed using a structured finite-volume flow solver utilising, in this work, the Reynolds-Averaged Navier-Stokes equations. The $k-\omega SST$ (Shear Stress Transport) turbulent model developed by Menter [50] was used.

Figure 9.2 illustrates the computational setup with the current settings consisting of a twin-plate with a length $L = 23.4$ mm. The thickness of the plates is 1.59 mm, constant along the x direction, with rounded off leading edge and with a sharp trailing edge, as described in Sreenivasan *et al.* [37]. The computational domain normalized by the twin-plate length ($45L \times 40L$) is also displayed in figure 9.2. The twin plate was aligned with the inflow and the Reynolds number based on the length of the twin-plate is $Re = 3.2 \times 10^4$, using an inflow velocity of 1 ms^{-1} and a density of 1 kg/m3. The computational setup of the CFD simulations consists of a mesh of one million 2D square

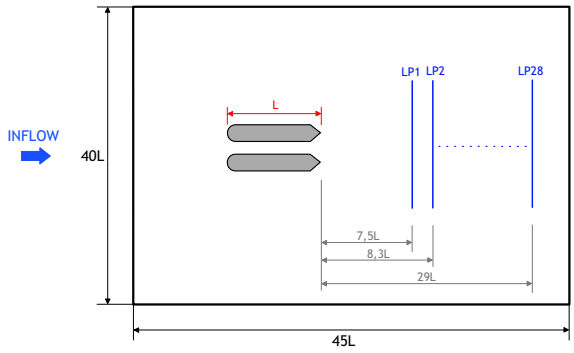

FIGURE 9.2: Computational domain (not to scale).

cells with the first cell height ($\Delta y/L$) of 5.85×10^{-5} normalized by the twin plate length. In order to obtain an optimal mesh, three refined volume meshes have been created, two of them around the plates and the third one behind the trailing edge of the plates, see Figure 9.3. In the immediate vicinity of the plates, the mesh has 0.5×10^6 cells, while the mesh downstream of the twin plate for capturing the wake has approximately 0.35×10^6 cells. In order to resolve the boundary layer, cell clustering has been used close to the wall and the dimensionless distance of the first layer of cells from the wall is less than 2 ($y+ < 2$), as is required by the *SST* turbulence model. Verification of sufficient mesh resolution was performed by a mesh independency study. Results obtained for the finest mesh were compared with the results for a standard and a coarse mesh. The deviation between the coarsest and the finest meshes indicates a difference of approximately 5% in the centreline wake defect velocity W_0.

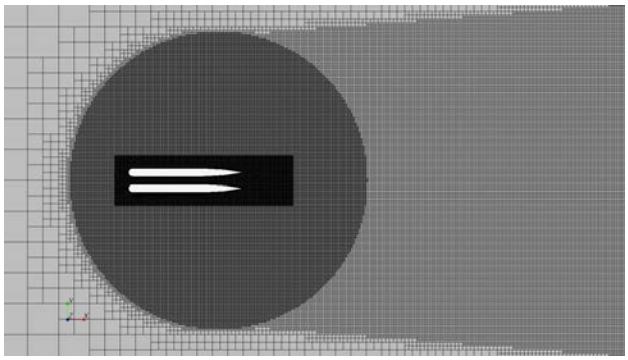

FIGURE 9.3: Mesh around the Twin-Plate

Data in the computational simulations were extracted in 28 streamwise lines, normal to the flow direction and located $x/L = 7.5 - 29$ plate lengths downstream the trailing edge of the twin-plates, as illustrated in Figure 9.2.

9.4 Results

A two dimensional numerical analysis was performed for the study of the twin-plate wake generator. Figures 9.4(a) and 9.4(b) represent the axial velocity field and the pressure field respectively. The plates were aligned with the oncoming flow in order to have an aerodynamic fashion lay-out and to subsequently be compared to the wind tunnel experiments and the analytical model described in Sreenivasan *et al.* [37]. The extraction of the velocities from the computations was conducted in a similar way to the experimental procedure, downstream of the twin-plate and applying cartesian coordinates to the velocity profiles with the origin in the middle point of the trailing edges of the plates.

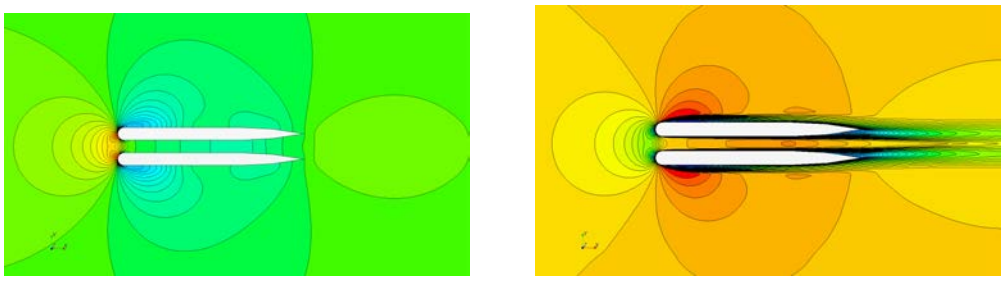

(a) Pressure field (b) Axial velocity field

FIGURE 9.4: Twin-plate pressure and velocity fields

9.4.1 Comparison with experimental data and the analytical model

Table 9.1 lists mean parameters of the twin-plate wake generator used in the experiments of Sreenivasan [53] for a comparison with the computational results. The momentum thickness θ is defined by the equation:

$$\theta = \int_{-\infty}^{+\infty} \frac{W}{U}\left(1 - \frac{W}{U}\right) dy \tag{9.9}$$

where W is the wake velocity deficit and U is the stream velocity outside the wake. The drag coefficient value of the computations matches quite well with the experimental one and the averaged momentum thickness is also very similar for both cases.

Additionally, the analytical model presented in Sreenivasan *et al.* [37] is considered for comparison. As explained in the *Section 9.1* and in the equations (9.8), it is useful to consider the development of two-dimensional turbulent wakes in term of the parameters described in the following two equations as a growth-rate expression (see also White [33]):

TWIN-PLATE CASE	C_D	$\overline{\theta}$ (mm)	Aspect Ratio	L (cm)	Re_L
Experimental	0.0740	0.874	64	2.33	3.2×10^4
CFD	0.0729	0.869	64	2.33	3.2×10^4

TABLE 9.1: Mean twin-plate wake parameters

$$\delta \approx 0.30\,(x\,\bar{\theta})^{\frac{1}{2}} \tag{9.10}$$

$$\frac{W_0}{U} \approx 1.63\left(\frac{\bar{\theta}}{x}\right)^{\frac{1}{2}} \tag{9.11}$$

where δ is the half-defect thickness, w_0/U is the center-line wake defect ratio and $\bar{\theta}$ the averaged momentum thickness measured in 28 line probes downstream of the twin plates.

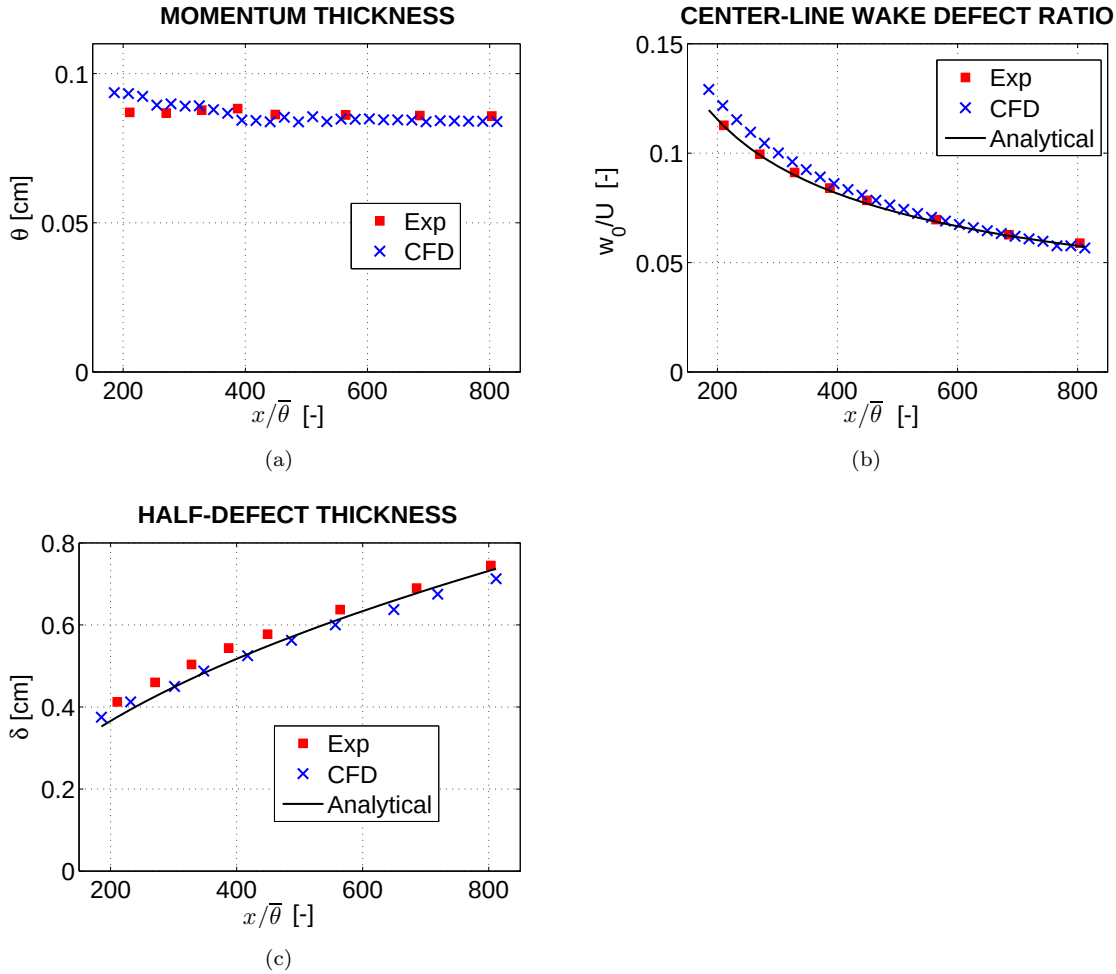

FIGURE 9.5: Twin-plate wake equilibrium parameters

Figure 9.5(a) displays the momentum thickness simulation results in a 2D wake behind a twin-plate of the computational simulations (x) and the comparison with experimental data (■). Note that, in the computations, a stable momentum is reached about 220 averaged momentum thicknesses downstream the dual-plate, while in the experiments the momentum was stabilized at about $\frac{x}{\theta} = 200$. Figures 9.5(b) and 9.5(c) display a comparison between the experimental and computational results for the calculations of the center-line wake defect and the shear layer half-defect thickness, respectively. In addition, the analytical model previously presented in the equations (9.10) and (9.11) has been represented. In both cases, a strong agreement is observed between the computational results and the ones of the experiments and the analytical model.

9.4.2 Testing of Self-similarity on two-dimensional twin-plate turbulent wake simulations

The twin-plate wake velocity components were extracted in 28 cross-planes positioned from 7.5 to 29 twin-plate lengths downstream of the trailing edges of the plates. Figure 9.6(a) shows the velocity profiles for all downstream positions with no scaling. Figure 9.6(b) illustrates that, if the twin-plate wake velocity profiles are correctly scaled, the curves collapse nicely verifying that self-similarity is achieved. A self-preserving state basically means that the mean velocity and the Reynolds shear stress distribution must be independent of the streamwise position when normalized by the same velocity and length scales. The developed self-similar region seems to grow from an apparent origin just behind the plates, between the trailing edges of the twin-plates. Downstream in the far wake, self-similarity is reached when equation (9.11) is fulfilled. It was observed in the computations that about 220 momentum thicknesses behind the dual plate, the velocity profiles become self-similar, which is quite similar to the value found in the experiments carried out by Sreenivasan [37]. Since there is no significant streamwise pressure gradient, the wake momentum thickness θ remains constant at each line probe position.

9.5 Conclusions

The two-dimensional turbulent wake behind a twin-plate has been numerically studied. Computational RANS simulations at Reynolds number $Re = 3.2 \times 10^4$ have been carried out and compared with experimental data and an analytical model.

The self-similar behaviour wake generated by the twin-plate was tested at 28 line positions x/L=7.5-29 plate lengths downstream the trailing edge. It was established that the

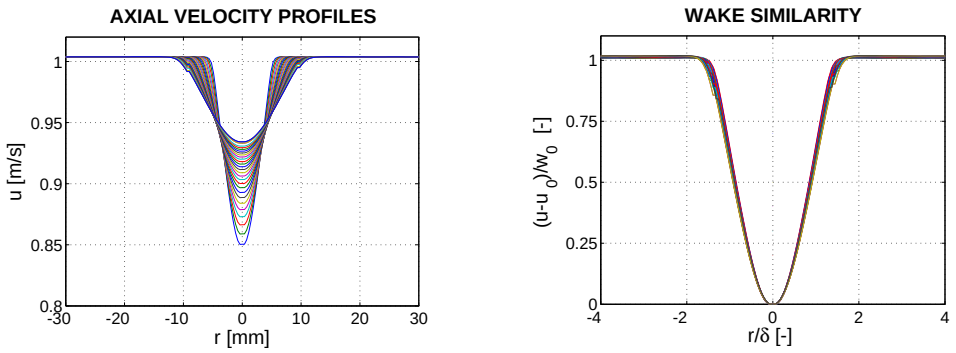

(a) Axial velocity profiles no scaled

(b) Axial velocity profiles scaled by self-similarity variables

FIGURE 9.6: Computational velocity profiles at positions x/L=7.5-29.

wake equilibrium was reached about 220 averaged momentum thicknesses downstream of the twin-plate. From the point of view of self-similarity, computational simulations are able to reproduce the physics of the flow behind the twin-plate with considerable reliability. The CFD results of Figure 9.5 match the experimental observations reasonably well, as well as the analytical model presented in [37].

For future investigations, it would be highly interesting to investigate the self-similar behaviour and the stability of the wake behind the twin-plate at higher Reynolds numbers and in three dimensions.

Chapter 10

Wake equilibrium parameters of symmetric airfoil simulations

In this chapter, a detailed computational study of the mean wake equilibrium parameters on a symmetric airfoil (NACA0012) is presented. Thus, steady state computational simulations at Reynolds number 10^6 have been carried out using Reynolds Averaged Navier-Stokes (RANS) equations and have been compared with the experimental data obtained by Hebbar [29] and the analytical model presented in Sreenivasan *et al.* [37]. The purpose of this work is to study the manner in which computational simulations on a symmetric airfoil at hight Reynolds number reproduce the wake development behind a NACA0012.

10.1 Introduction

The dynamic characteristics of the pressure and velocity fields of turbulent wakes behind an airfoil are investigated numerically and analyzed from a physical point of view.. The flow in the near wake of an airfoil significantly affects the airfoil pressure distribution and hence is of considerable interest. Townsend [24], Harsha *et al.* [25] and Marvin [54] conducted an experimental study of turbulence modeling for external aerodynamic flows where self-similar behaviour behind different wake generators was made. Chevray and Kovasznay [55] made also some turbulence measurements on the wake of a thin flat plate. Later, Hebbar [29] investigated the boundary layer and wake development parameters on a symmetric airfoil where detailed measurements of two−dimensional profiles of static pressure, mean velocity, turbulence intensity and Reynolds shear stress were analyzed. Fernández-Gámiz *et al.* [31] and Velte [4] also investigated numerical and experimentally the self-similar manners of the wake on a rectangular vortex generator on a flat plate.

Furthermore, a numerical analysis of two dimensional mean velocity profiles downstream of a twin−plate was carried out by Fernández-Gámiz *et al.* [52]. As described in the previous chapter and according to George [32], a self-preserving state on a flow exists when in the evolution of the wake, see Figure 10.1(a). All dynamical parameters have the same relative value at the same relative position. These parameters are sketched in Figure 10.1(b), where U_∞ is the free stream velocity, u_0 the convection velocity and W_0 and δ the defect velocity and the half-defect thickness, respectively.

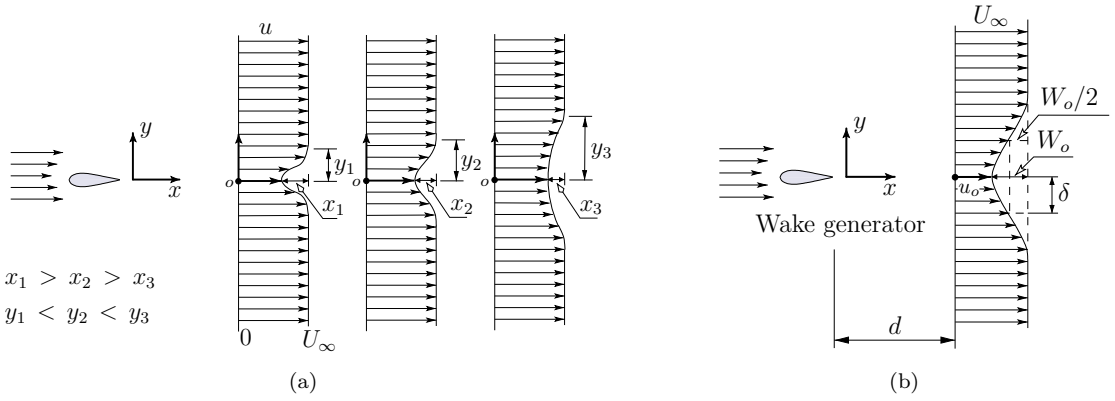

FIGURE 10.1: Wake development parameters behind a symmetric airfoil.

10.2 Experimental data

The experimental data for this work is the one of Hebbar [29]. The experiments were carried out in the National Aeronautical Laboratory Boundary Layer Tunnel of Bangalore (India). It is a low speed, blower type, open circuit wind tunnel with a 9.6 m long closed test section of nominal cross section of 1.3 m wide and 0.3 m high with the maximum test section velocity of 50 ms^{-1} and a longitudinal intensity of the freestream turbulence of less than 0.1%. The Reynolds number based on the chord length of c=600 mm was one million and the wake measurements extended up to three chord lengths downstream of the trailing edge of a symmetric airfoil NACA0012. The instrumentation included in the experiments consisted of a boundary layer Pitot probe, a conventional static probe, a disk-type static probe, a single wire and an x-wire probe. The experimental setup of the streamwise measuring stations and flow configuration is sketched in Figure 10.2. More detailed information about the experiments can be found in Hebbar [56].

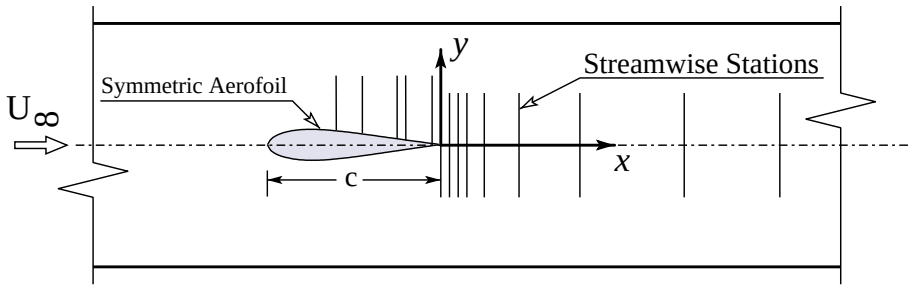

FIGURE 10.2: Flow configuration and streamwise measuring stations.

10.3 Computational Configuration

In this study, two-dimensional steady state simulations have been carried out and compared to the previous experimental observations. The computations were performed using a structured finite-volume flow solver utilising, in this work, the Reynolds-Averaged Navier-Stokes RANS equations. The $k-\omega$ *SST* Shear Stress Transport turbulence model developed by Menter [50] was used.

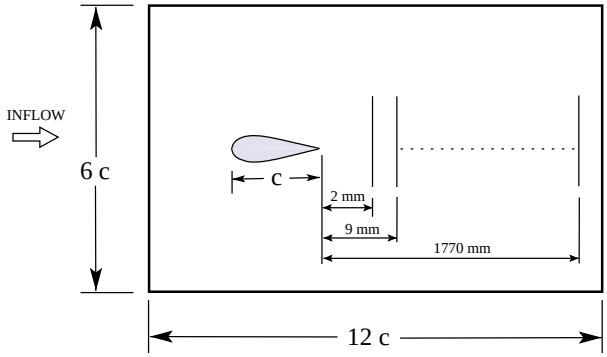

FIGURE 10.3: Computational domain and streamwise measuring stations (not to scale).

The computational setup of a symmetric airfoil with a chord length $c = 600$ mm, 30 cm span, 12.5 relative thickness-to-chord ratio and 1.5 mm trailing-edge thickness together with the streamwise measuring stations is sketched in Figure 10.3. The computational domain has been normalized by the airfoil chord length ($6c$ x $12c$). The airfoil angle of attack was aligned with the oncoming flow and the Reynolds number based on the airfoil chord length is $Re = 10^6$, using an inflow velocity of 1 ms^{-1} and a density of 1 kg m^{-3}. The mesh consists of a half million 2D square cells with the first cell height ($\Delta y/c$) of 2.21x10^{-6} normalized by the airfoil chord length. In order to obtain an optimal mesh, three refined volume meshes have been created, two of them around the airfoil and the third one behind the trailing edge of the airfoil to capture the full development of the wake. This particular mesh has approximately 417497 nodes and 414824 2D square cells with considerable mesh concentration both around the airfoil and in the near wake region, see Figure 10.4.

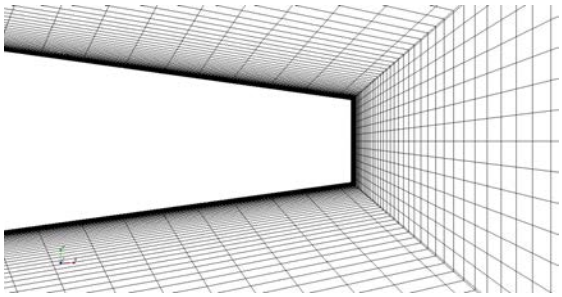

FIGURE 10.4: Mesh on the airfoil trailing edge.

In order to resolve the boundary layer, cell clustering has been used close to the wall and the dimensionless distance of the first layer of cells from the wall is less than 2 ($y^+ < 2$), as is required by the SST turbulence model. Data in the computational simulations were extracted in 12 streamwise plane positions, normal to the flow direction and located at various distances downstream the trailing edge of the airfoil, as illustrated in Figure 10.3. In the computations, wake measurement stations extended up to three chord lengths behind the trailing edge of the airfoil.

10.4 Results

A two−dimensional computational study has been performed to analyze a symmetric airfoil wake. Figures 10.5(a) and 10.5(b) represent the steady axial velocity field and the pressure field, respectively. The extraction of the velocities from the computations was conducted in a similar way to the experimental procedure, downstream of the airfoil and applying cartesian coordinates to the velocity profiles with the origin in the middle point of the trailing edges of the airfoil.

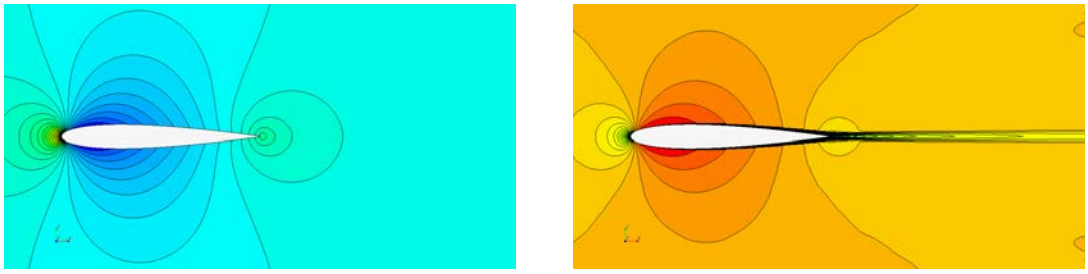

(a) Pressure field

(b) Axial velocity field

FIGURE 10.5: Airfoil pressure and velocity fields

Figure 10.6 shows the computational results of the streamwise development of the half wake profiles in every plane position downstream the airfoil, from x=2 mm to x=1770 mm. Figure 10.7 represents a comparison between the mean velocity profiles on either side of the wake at 2 mm downstream of the trailing edge. Since the maximum difference

between the mean velocity profiles is less than 0.25%, the symmetry of the wake at this station is considered quite good.

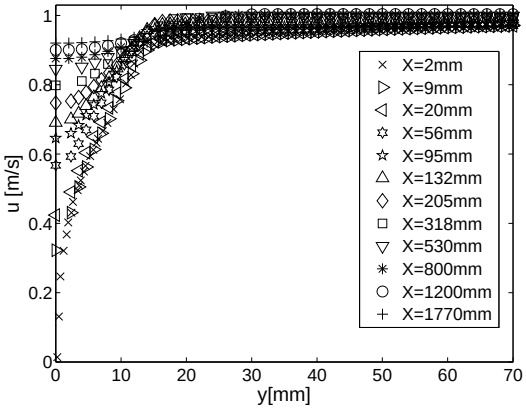

FIGURE 10.6: Mean velocity computational profiles on the NACA0012 airfoil wake.

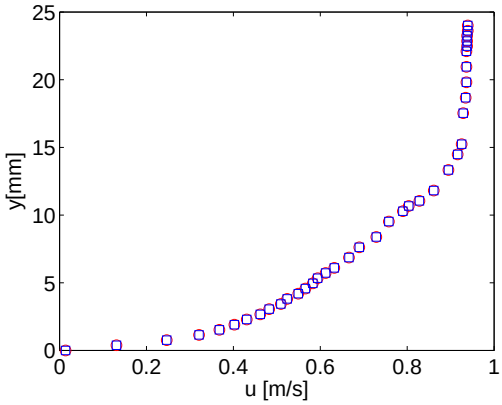

FIGURE 10.7: Comparison of mean velocity computational profiles on either side of the wake.

10.4.1 Comparison with experimental data and the analytical model

The overall characteristics of the mean flow field of the wake are presented in Figures 10.8, 10.9 and 10.10. Figure 10.8 displays the momentum thickness CFD results on the 2D wake behind the NACA0012 airfoil. The momentum thickness θ is defined by the equation (9.9), where W is the wake velocity deficit and U is the stream velocity outside the wake. $\bar{\theta}$ is the averaged momentum thickness, calculated as the averaged value once the equilibrium is reached and correspond to $\bar{\theta}$= 1.497 in the computations. At large distances ($x/\bar{\theta} > 400$) from the trailing edge of the airfoil the structure of the mean flow is expected to reach a state of self−preservation asymptotically. The approach to equilibrium of this study is examined in terms of equilibrium parameters for two-dimensional wakes as defined in Prabhu [27]. Furthermore, the analytical model presented in Narasimha *et al.* [28] is considered for comparison with the computational results. As explained in the *Section 9.1* and in the equations (9.8), it is useful to consider the development of two-dimensional turbulent wakes in term of the parameters described in the equations (9.10) and (9.11).

As expected, in the region close to the trailing edge, where the distance is less than 200 times the averaged momentum thickness, the value of the momentum thickness decreases with downstream distance. Further downstream, the value of θ tends to approach a constant value. Note that a stable momentum is reached at the station $x/\bar{\theta} \approx 350$. Since there is no significant streamwise pressure gradient, the wake momentum thickness θ seems to be constant. Figure 10.9 represents the center line wake defect evolution downstream the trailing edge of the airfoil for the computations against the experiments and

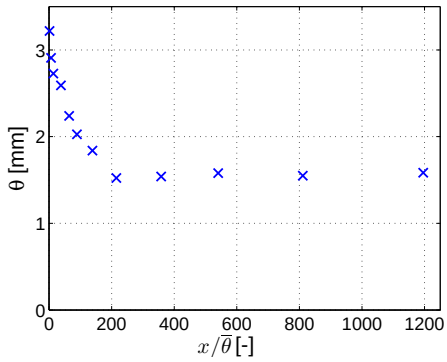

FIGURE 10.8: Momentum thickness evolution on the Wake profiles (CFD results).

the analytical model both previously mentioned. The center line wake defect ratio for the analytical model is defined by the equation (9.11). The center line wake defect ratio is quite large in the beginning, very close to the trailing edge, but decreases immediately and tends to approach a constant value in the far wake region. Figure 10.10 displays a comparison of the shear layer half-defect thickness along the wake evolution between the computations and the wind tunnel measurements already referred. Further, the analytical model for describing the half-defect thickness development presented in Narasimha *et al.* [28] and defined by the equation equation (9.10) has been implemented. In general, the numerical results predict quite well the experimental ones. Nevertheless, divergences are notable when predicting the wake half-defect thickness.

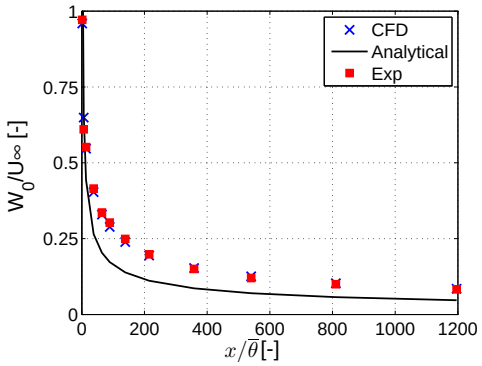

FIGURE 10.9: Center line wake defect ratio evolution.

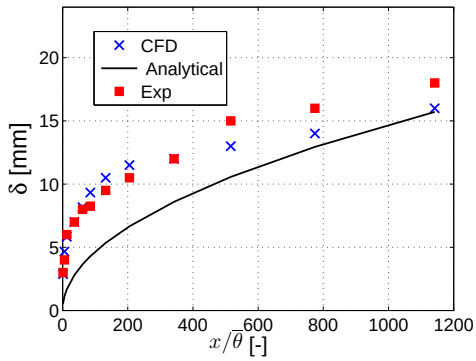

FIGURE 10.10: Half−defect thickness in the wake evolution.

Figure 10.11 represents a comparison between experimental data (■) and computational results (X) at the stations $x = 2 - 1770$ mm downstream of the trailing edge of the NACA0012 airfoil. In each plot, the half-wake velocity profile at a particular plane position downstream the airfoil is represented and compared with experimental data obtained from Hebbar [29]. In general, a notable agreement is observed between the computational results and the ones of the experiments. However, some discrepancies

are visible in the near wake area. For the plane position of x=2 mm the peak of the velocity near to the undisturbed area is not captured in the computations. Far from the trailing edge the computational simulations capture the evolution of the wake with high reliability.

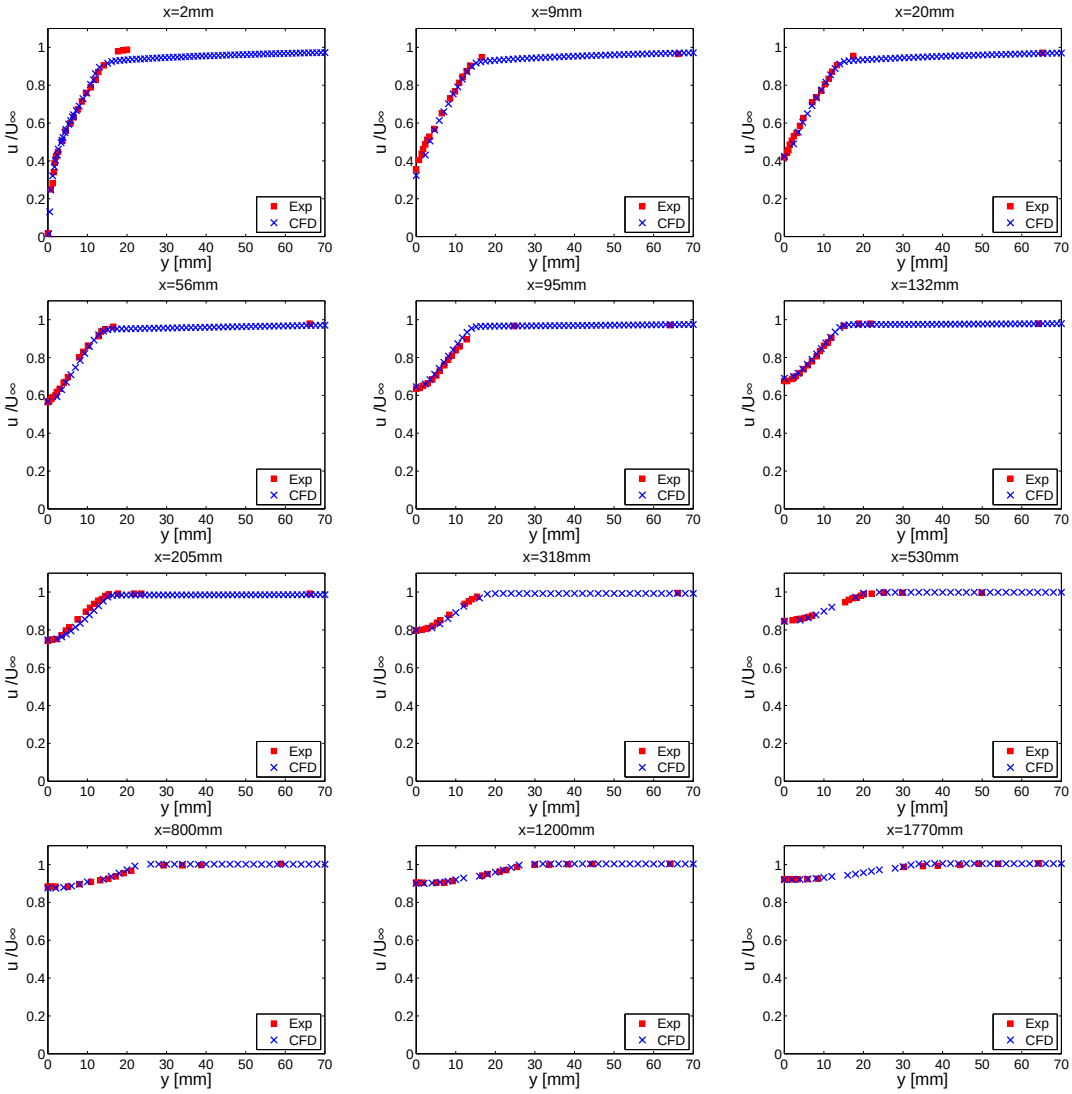

FIGURE 10.11: Comparison between experimental data (■) and computational results (X) at the plane positions $x = 2 - 1770$mm downstream of the trailing edge.

10.4.2 Testing of Self-similarity on a two-dimensional NACA0012 turbulent wake simulations

The symmetric airfoil wake velocity profiles were extracted in 12 cross planes positions, as sketched in Figure 10.4, and the results have been represented in Figure 10.6. If the airfoil wake velocity profiles are conveniently scaled, self-similarity can be reached in the far wake. In a self-preserving state the mean velocity and the Reynolds shear stress distribution must be independent of the streamwise position when normalized by the same velocity and length scales. Figure 10.12 shows the non-dimensional mean velocity wake defect defined by $\left[\frac{1-\frac{u}{U_\infty}}{1-\frac{u_0}{U_\infty}}\right]$, where u_0 is the wake convection velocity, versus the normal distance from the wake center line y normalized by the half-wake width δ, as sketched in Figure 10.1(a). In this study, the approach to wake equilibrium has been examined in terms of equilibrium parameters for two-dimensional waked defined in Prabhu [27] and Sreenivasan *et al.* [37]. Note that, in Figure 10.12, only the velocity profiles of the far wake where $\frac{x}{\theta} > 350$ have been represented, i.e., from x=530 to x= 1770 mm. Also included in the figure for comparison is represented the Gaussian distribution of the mean velocity profiles defined after $2^{-(\frac{y}{\delta})^2}$.

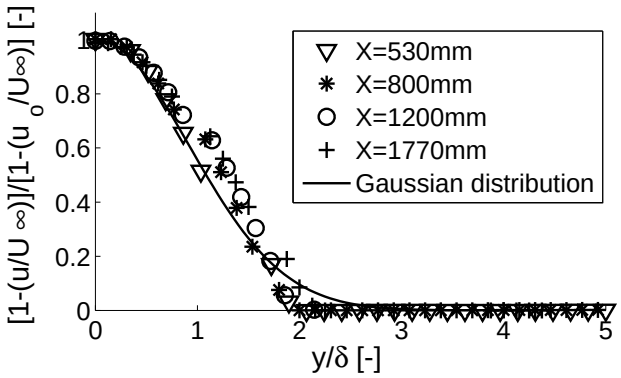

FIGURE 10.12: Non-dimensional mean−velocity defect distribution in the far wake.

10.5 Conclusions

The two-dimensional turbulent wake downstream of a symmetric airfoil NACA0012 has been studied. Computational RANS simulations at Reynolds number based on the airfoil chord length $Re = 10^6$ have been carried out and compared with experimental data from Hebbar [29] as well as with the analytical model for two-dimensional turbulent wakes presented in Narasimha *et al.* [28]. The wake profile parameters generated by the symmetric airfoil has been tested at 12 plane positions x=2-1770 mm downstream the trailing edge. As Figure 10.11 illustrates, the computational results match reasonably

well with the experimental observations. However, some differences in the near wake profiles are visible. This deviation between the CFD and the experimental results could be attributed to the lack of two-dimensionality in the flow field measurements and a favorable pressure gradient induced by flow convergence in the wind tunnel, as emphasized in Hebbar [29]. In the computations it has established that the wake equilibrium is reached at the the station $x \approx 600$mm (around 400 averaged momentum thicknesses) downstream of the airfoil. From the point of view of self-similarity, the mean velocity profiles of the computational simulations seems to collapse in the far wake and tend to approach similarity form.

Part V

Summary and Future Work

Chapter 11

Summary

In this chapter, a summary of the main conclusions of each part of this thesis is presented. Chapter 12 recommends follow-up topics to the current work.

11.1 Summary of Part II

A new numerical Actuator VG model (AcVG) model has been implemented in the EllipSys CFD code to simulate vortex generator flow. The results are validated against experimental data and an analytical model. This new model is based on the principle of the BAY model and has been integrated into the code as a source term in the momentum and energy equations. The novelty of this implementation consists of the application of the local forces in the cells just in the outline of the VG geometry, instead of applying the forces in all the cells of the subdomain, as defined in the BAY model. Further, the AcVG model has been compared to a fully resolved vortex generator geometry. Regarding to the computational time, the mesh-resolved VG model time has been estimated three hundred times bigger than the Actuator VG model time. Thus, from the point of view of the computational effort, the efficiency of the AcVG model is much higher than the mesh-resolved VG. A significant reduction in cells has been also achieved by replacing the detailed VG boundary layer mesh by the new modelling method. Once the vortex produced by the mesh-resolved VG is fully developed at around 10 VG heights downstream the trailing edge of the VG, the AcVG model matches the vortex generated by the mesh-resolved VG model. It has been demonstrated that it saves both meshing and computational time. We can also confirm that the analytical model developed by [36] can be used as a calibration tool for the AcVG model. This Actuator VG model could easily be applied for complementing full rotor computation and for doing parametric

study of the VG layout. The potentially open applications of the Actuator VG model are several.

Further, in this part, angle dependency of vortices generated by a passive rectangular vane-type vortex generator of the same height as the boundary layer thickness in a flat plate have been studied. CFD computational simulations with four different angles of attack β ($20°, 25°, 30°$ and $35°$) of the VG to the oncoming flow have been carried out using the RANS method and compared with wind tunnel experimental data and an analytical model. Nevertheless, significant differences between the numerical simulations and the measurement results were observed as the angle of attack increased. Several factors can explain these discrepancies. One reason for these differences could be that the boundary layer evolution along the wall was not accurately performed in the simulations to reproduce the same boundary layer profile facing the leading edge of the VG as in the wind tunnel experiments. At 20 degrees of angle of attack the CFD results are well matched with wind tunnel experimental data and the analytical model, both for the axial and azimuthal velocity profiles. Furthermore, the vortex convection velocity in both cases matches very well. However, the perturbation from a secondary vortex, which is observed in the asymmetry to the right in the axial velocity profiles, seems to be stronger in the CFD case. This secondary vortex is present with variable strength at all considered device angles, introducing a disturbance in the flow field of the main vortex. However, the influence is more notable in the 20 degrees case. In the 25 degrees of angle of attack case, the axial velocity profiles show acceptable agreement in all the cases, though the azimuthal velocity profile of the CFD case starts displaying relevant differences with the wind tunnel data and the model. These discrepancies become larger with increasing vane angle. For all four VG angles it is seen that the axial velocity is predicted much better than the azimuthal one. In the azimuthal profiles, it is evident that the swirl increases with increased angle of attack. Unfortunately, the CFD simulations are not able to accurately capture this increase. These differences in the azimuthal velocity profiles could be explained due to the difficulties of the turbulent models to capture the swirling flows with high accuracy.

11.2 Summary of Part III

Self-similarity and helical symmetry of vortices generated by a passive rectangular vane-type vortex generator of the same height as the boundary layer thickness on a test section wall have been studied. CFD simulations at Reynolds number Re=1700 have been carried out using the RANS method and compared with corresponding wind tunnel

experimental data and an analytical model. The vortex generated by the VG flow simulations shows self-similar behaviour for both the axial and azimuthal velocity profiles. It was shown based on data from five plane positions z/h = 5, 7.5, 10, 12.5, 15 downstream of the trailing edge of the VG and with the angle of attack β=20^o of the vane to the oncoming flow. Though the simulations are not able to reproduce the same absolute values as in the experiments, the helical symmetry of the main vortex generated by a rectangular VG has been tested and compared with the analytical model developed in [36] with good agreement. Self-similarity behavior has also been confirmed in several positions downstream of the VG computational simulations. Furthermore, four characteristic vortex parameters have been analyzed: convection velocity, circulation, helical pitch and vortex core radius. The trends of these parameters of the computational simulations are in line with the ones shown in the experiments of [3].

In general, the simulations are able to reproduce the physics of the flow downstream of the VG. The CFD results show relatively good agreement with the self-similarity shown in the experiments carried out in [4] and the trends of the characteristic helical vortex parameters in the computational results match the experimental observations of [36] reasonably well. From the point of view of self-similarity, computational simulations are able to mimic the physic of the vortex generated by a rectangular VG with reliably. The helical symmetry has been also tested and verified based on the computational data.

11.3 Summary of Part IV

This part contains a detailed two-dimensional computational analysis of self-similarity and wake equilibrium parameters behind two different wake generators: a twin−plate and a symmetric airfoil.

Firstly, a two-dimensional turbulent wake behind a twin-plate has been numerically studied. Computational RANS simulations at Reynolds number $Re = 3.2 \times 10^4$ have been carried out and compared with experimental data and an analytical model. The self-similar behaviour wake generated by the twin-plate has been tested at 28 positions x/L=7.5-29 plate lengths downstream the trailing edge. It was established that the wake equilibrium was reached about 220 averaged momentum thicknesses downstream of the twin-plate. From the point of view of self-similarity, computational simulations are able to reproduce the physics of the flow behind the twin-plate with considerable reliability. There is a good consistency between the CFD results and the experimental observations, as well as with the analytical model presented in Narasimha *et al.* [28].

The second case consists of a two-dimensional symmetric airfoil computational domain. Computational RANS simulations at Reynolds number based on the airfoil chord length $Re = 10^6$ have been carried out and compared with experimental data from Hebbar [29]. Additionally, the analytical model previously mentioned [28] has also been introduced for comparison. The wake profile parameters generated by the symmetric airfoil has been analyzed at 12 different stations x=2-1770 mm downstream the trailing edge and compared with the measurements. Divergencies has been detected in the near wake velocity profiles comparison between the simulations and the measurements. It has been determined in the computations that the wake equilibrium state seems to be reached at the the station $x/\bar{\theta}$ ≈400 downstream of the airfoil. As Figure 10.12 illustrates, the mean velocity profiles of the far wake seems to collapse.

The computational results indicate significant changes in the flow parameters close to the airfoil trailing edge, however the relaxation of the wake is reached after the initial overshoot in the streamwise profiles of the mean flow parameters. The twin-plate wake appears to have more simple behaviour than the symmetric airfoil wake and attains self-preservation state in shorter distance, as was suggested in Narasimha *et al.* [28].

Chapter 12

Future work

During the course of this research work and after many passionate discussions with many researchers, several ideas have emerged, which unfortunately due to the limitation of time and facilities could not always be pursued. In this chapter, some suggestions and recommendations are presented for further development of the current work.

For future investigations, it would be highly interesting to continue the investigation of the evolution of the induced vortices on the wakes of vortex generators simulations. More computational simulations with LES/DES models are also recommended to carry out. These mathematical models for turbulence could provide more practical information about vortices generated by the VGs.

About the implementation of the BAY model, the principal purpose of the use of this model for wind turbine blades is to efficiently determine the optimum VG lay-out. The BAY model can, of course, only provide significant qualitative information on VG array designs for blades if the confidence on applying the BAY model is trustworthy. In the present work, only one baseline vortex generator on a flat plate has been validated with the mesh resolved VG model and with experimental data. Therefore, for future research more validation cases of the BAY model are recommended; even more investigations about the Actuator VG model (AcVG) calibration dependency of the Reynolds number and the inflow angle are needed.

It would also be interesting to conduct more extensive experiments. It might include experimental SPIV investigation and computational simulations of vortex generator rows on prismatic airfoils at different stations from the leading edge and a quantification of the impact of the vortex generators by the use of three-dimensional Proper Orthogonal Decomposition (POD) of the flow field. More experiments at higher Reynolds number and comparison with numerical simulations and even with adverse pressure gradients

are also recommended in order to reproduce a more realistic flow conditions. In fact, these experiments have already been performed in the large wind tunnel for boundary layer in the Laboratoire de Mcanique de Lille (France) and are under processing.

Finally, in order to find the most optimum VG geometry and to study the different impact of these devices in the boundary layer motion, some new fashion geometries are proposed, see Figure 12.1. These new VG shapes have been designed with the main objective to reduce the drag penalty associated to passive vortex generators at small angles of attack. Therefore, new experiments and computations are required to evaluate the aerodynamic performance of these VG shapes.

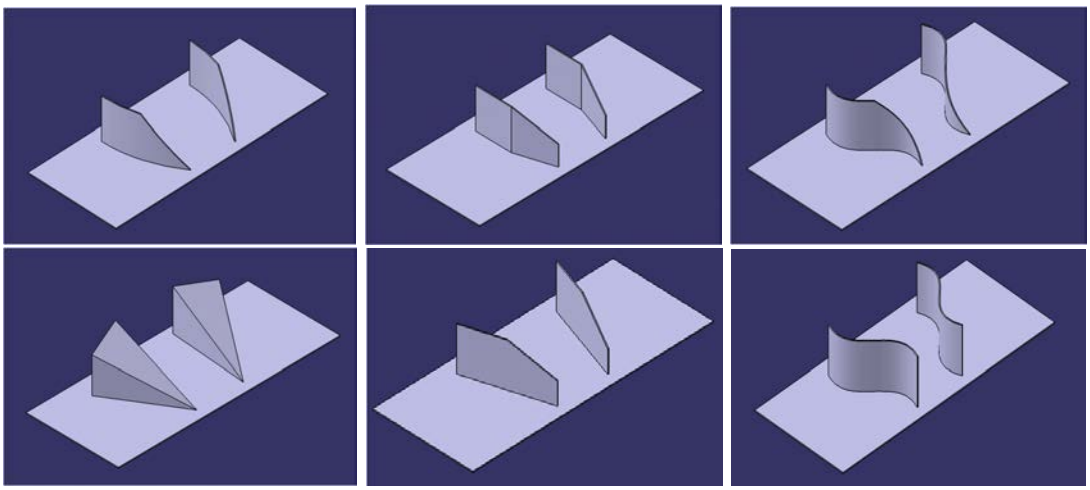

FIGURE 12.1: Different VG geometries.

Part VI

Appendices

Appendix A

Computational Fluid Dynamics Codes

Numerical simulations presented in this work in Part II: Vortex Generators Models and Part III: Testing of Self-similarity and Helical symmetry have been carried out by the EllipSys3D CFD code developed at Risø-DTU Technical University of Denmark (Michelsen [34, 57], Sørensen [35])

The EllipSys3D is a flow solver CFD Code, with a multiblock finite volume discretization of the incompressible Reynolds Averaged Navier-Stokes (RANS) equations. The EllipSys solution sequence is explained in the scheme of Figure A.1

The Rhie-Chow [58] interpolation scheme was used and the parameters are solved on collocated meshes in primitive variables. Several spatial discretitation schemes are available (upwinding, central and second order upwinding). All simulations presented in Part II and III have been performed using the third order Quadratic Upstream Interpolation for Convective Kinematics (QUICK) upwind scheme implemented by the approach of [49]. Pressure-velocity coupling is undertaken by SIMPLE/PISO algorithms.

This code is programmed in Fortran 95 and parallelized with the Mesage-Passing Interface MPI (for more detailed information see the MPI standard in: http://www-unix.mcs.anl.gov/mpi/) for executions on distributed memory machines, using a non-ovelapping domain decomposition technique. Computations were made by use of Thyra PC-cluster at DTU-Risø Campus. Since the EllipSys code is considered confidential and has copyright and protection under law, additional information may be obtained from the author.

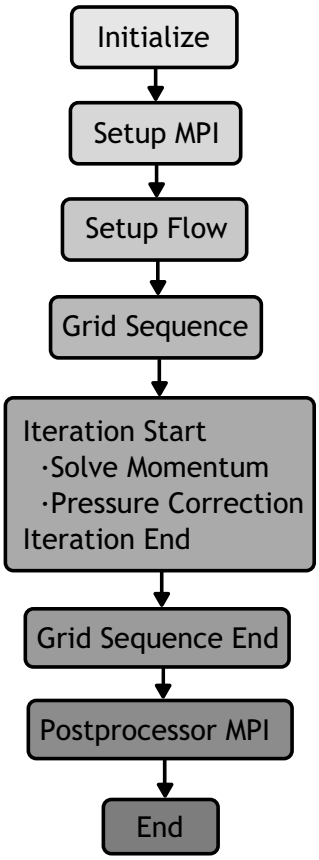

FIGURE A.1: EllipSys CFD code solution sequence

Numerical simulations carried out in Part IV: Self-similarity and Wake Equilibrium Analysis on Two-dimensional Turbulent Wakes. of this work have been done by StarCCM+v8-R8 double precision CFD code developed by CD-ADAPCO (www.cd-adapco.com). This code provides a range of state of the art models; Spalart-Allmaras, a range of K-ε models, both standard and SST variants of the K-ω model as well as two Reynolds stress models. Where laminar-turbulent transition occurs, STAR-CCM+ has the option to use the Gamma-Re-Theta model to model its onset. Computations were made by use of Arina cluster at the university of the Basque Country with technical and human support provided by IZO-SGI, SGIker (UPV/EHU, MICINN, GV/EJ, ERDF and ESF)

Appendix B

Governing Equations

B.1 Reynolds averaged Navier-Stokes equations

The Navier-Stokes equations describe the motion of fluid particles. These equations arise from applying Newton's second law to fluid motion, together with the assumption that the stress in the fluid is the sum of a diffusing viscous term (proportional to the gradient of velocity) and a pressure term- hence describing viscous flow. The NavierStokes equations are nonlinear partial differential equations in almost every real situation, [59, 60]. In some cases, such as one-dimensional flow and Stokes flow (or creeping flow), the equations can be simplified to linear equations. The nonlinearity makes most problems difficult or impossible to solve and is the main contributor to the turbulence that the equations model. The nonlinearity is due to convective acceleration, which is an acceleration associated with the change in velocity over position. Hence, any convective flow, whether turbulent or not, will involve nonlinearity [61].

The incompressible Navier-Stokes equations are:

$$\frac{\partial u_i}{\partial xi} = 0; \qquad \rho\frac{\partial u_i}{\partial t} + \rho u_j\frac{\partial u_i}{\partial x_j} = -\frac{\partial p}{\partial x_i} + \frac{\partial t_{ji}}{\partial x_j} \tag{B.1}$$

where ρ is the density, x_i the coordinate in i direction and t_{ji} the viscous stress tensor.

To solve these equations for incompressible flow, velocity and pressure are considered as:

$$u_i(x_i, t) = U_i(x_i) + u_i^{'}(x_i, t) \tag{B.2}$$

$$p(x_i, t) = P(x_i) + p^{'}(x_i, t) \tag{B.3}$$

where uppercase letters represent the mean part and the prime represents the mean value fluctuation of the variables. The mean part is a time averaged variable.

If the equations B.2 B.3 are substituted in B.1, the resulting equations are the time averaged:

$$\frac{\partial U_i}{\partial xi} = 0; \qquad \rho\frac{\partial U_i}{\partial t} + \rho U_j\frac{\partial U_i}{\partial x_j} = -\frac{\partial P}{\partial x_i} + \frac{\partial(2\mu S_{ji} - \rho\overline{u_j^{'}u_i^{'}})}{\partial x_j} \tag{B.4}$$

The resulting equations B.4 are the Unsteady Reynolds Averaged Navier-Stokes (URANS) equations but if one can assume that the flow is steady the time derivative can be neglected and then the Reynolds Averaged Navier-Stokes (RANS) equations can be obtained.

B.2 Turbulence models

In this work, the Shear Stress Transport model (SST) is used which is a blend of two turbulence models: the $k-\epsilon$ model and the $k-\omega$ model. While the ϵ equation has been successfully applied to many industrial CFD cases, often in combination with wall functions; in the present work ω equation has been used because it offers a more accurate and robust modelling framework for boundary layers. The deficiencies of the ϵ in this respect are well known, namely a much too weak response to adverse pressure gradients and thereby a strong tendency to miss or under-predict separation of flow. This is an important issue, as it results in overly optimistic loss/stall predictions, leading the design tool to belief the flow is attached when in reality it is already in a range with large separation related losses.

B.2.1 $k-\epsilon$ model

The $k-\epsilon$ model relates the eddy viscosity ν_T, the turbulent kinetic energy k and the dissipation rate ϵ:

$$\mu_T = \rho\, C_\mu \frac{k^2}{\epsilon} \tag{B.5}$$

The transport equations for turbulent kinetic energy k and turbulent dissipation rate ϵ are defined bye the equations B.6 and B.7, respectively:

$$\rho\frac{\partial k}{\partial t} + \rho U_j\frac{\partial k}{\partial x_j} = \tau_{ij}\frac{\partial U_i}{\partial x_j} - \rho\epsilon\omega + \frac{\partial}{\partial x_j}\left[\left(\mu + \frac{\mu_t}{\sigma_k}\right)\frac{\partial k}{\partial x_j}\right] \tag{B.6}$$

$$\rho\frac{\partial \epsilon}{\partial t} + \rho U_j\frac{\partial \epsilon}{\partial x_j} = C_{\epsilon 1}\frac{\epsilon}{k}\tau_{ij}\frac{\partial U_i}{\partial x_j} - C_{\epsilon 2}\rho\frac{\epsilon^2}{k} + \frac{\partial}{\partial x_j}\left[\left(\mu + \frac{\mu_t}{\sigma_\epsilon}\right)\frac{\partial \epsilon}{\partial x_j}\right] \tag{B.7}$$

with the following values of the coefficients:

$$C_{\epsilon 1} = 1.44;\quad C_{\epsilon 2} = 1.92;\quad C_\mu = 0.09;\quad \sigma_k = 1.0;\quad \sigma_\epsilon = 1.3 \tag{B.8}$$

The $k-\epsilon$ model is widely used in plenty of CFd applications due to a low cost-effectiveness, however this model is very sensitive to adverse pressure gradients and the prediction of the viscous layer is very poor.

B.2.2 $k-\omega$ model

Similar to the $k-\epsilon$ model, the $k-\omega$ model relates the eddy viscosity ν_T to the turbulent kinetic energy k but uses a different dissipation rate the ω:

$$\mu_T = \rho\frac{k}{\omega} \tag{B.9}$$

The transport equations for turbulent kinetic energy k and turbulent dissipation ratio ω are defined bye the equations B.10 and B.11, respectively:

$$\rho\frac{\partial k}{\partial t} + \rho U_j\frac{\partial k}{\partial x_j} = \tau_{ij}\frac{\partial U_i}{\partial x_j} - \beta'\rho k\omega + \frac{\partial}{\partial x_j}\left[\left(\mu + \frac{\mu_t}{\sigma_k}\right)\frac{\partial k}{\partial x_j}\right] \tag{B.10}$$

$$\rho\frac{\partial \omega}{\partial t} + \rho U_j\frac{\partial \omega}{\partial x_j} = \alpha\frac{\omega}{k}\tau_{ij}\frac{\partial U_i}{\partial x_j} - \beta\rho\omega^2\omega + \frac{\partial}{\partial x_j}\left[\left(\mu + \frac{\mu_t}{\sigma_\omega}\right)\frac{\partial \omega}{\partial x_j}\right] \tag{B.11}$$

The $k-\omega$ model is more accurate in the near wall modelling compared to the $k-\epsilon$ model; the $k-\omega$ model has shown a disturbing sensitivity to the freestream values for ω at the boundary layer edge, through the inlet values (Menter [62]). The resulting base line model which combines the advantages of the ϵ and ω equations (Menter [50]), serves today as the basis of many turbulence models, like the Shear Stress Transport

(SST) model, which has gained widespread usage in aerodynamics and general CFD applications.

B.2.3 Shear Stress Transport model

The Shear Stress Transport model (SST) was proposed by Menter [50] as a combination between the $k-\epsilon$ model and the $k-\omega$ model. The blending of the turbulence modes is achieved by multiplying a transformed form of $k-\epsilon$ model and the $k-\omega$ model by the factors (F_1) and ($1-F_1$), respectively. F_1 is a blending function between one and zero depending fo the distance from the wall. The value one corresponds to the the position at the wall and the value zero at a distance from the wall. As a results, $k-\omega$ model is used close to the wall, in the boundary layer a combination of the $k-\epsilon$ and the $k-\omega$ models and outside the boundary layer only the $k-\epsilon$ model is adopted. A general description of the implementation of SST model in the ElliSys CFD code is described in [35].

Appendix C

Mesh Dependency Study

In CFD simulations, results are very dependent on the grid quality. By changing the cell size and/or grid structure divergent solutions can be obtained. Therefore, a mesh study must be performed to validate the results obtained with a mesh. All flow filed parameters should be asymptotically converge to a value for decreasing cell size. When this tendency is found, the mesh is started to be appropriated. Usually computational resources are expensive and limited, so reasonable small cell sizes are in favour. However the mesh should be large enough such the solution is located in the asymptotic region for convergence. A extended guide about grid dependency studies is given in Stern *et al.* [43].

In the computational simulations used for this thesis three grids are always involved (according to Stern et al [43], a convergence study requires a minimum of three grid solutions): a very coarse (h_3), a coarse (h_2) and a fine (h_1). The (h_2)-grid has half the cells of (h_1)-grid, in each direction and the (h_3)-grid has half the cells of (h_2)-grid, in each direction. Furthermore, as recommended, geometrically similar grids are used along with structured grid refinement.

Richardson extrapolation (Richardson *et al.* [42]) is usually used to calculate a higher-order estimate of the flow fields from a series of lower-order discrete values. For the case of grid refinement study, the value estimated from the Richardson extrapolation is the value that would results if the cell grid size tended to zero, ($h \to 0$). The extrapolation is made from the results of at least two different grid solutions.

In this research work, a generalized Richardson extrapolation form performed by Roache [63] has been followed. Thus, the mesh refinement ratio r is defined as:

$$r = \frac{h_2}{h_1} \tag{C.1}$$

A ratio of two or more is generally recommended. Defining f as a solution of the flow, the errors between the grids are calculated by the variables ϵ_{21} and ϵ_{32}:

$$\epsilon_{21} = f_2 - f_1 \tag{C.2}$$

$$\epsilon_{32} = f_3 - f_2 \tag{C.3}$$

To evaluate the extrapolated value from these solutions, the convergence conditions of the system must be first determined. The possible convergence conditions are:

- Monotonic convergence $\Rightarrow 0 < R < 1$
- Oscillatory convergence $\Rightarrow R < 0$
- Divergence $\Rightarrow R > 1$

The ratio R is defined by the errors calculated in (C.2) and (C.3):

$$R = \frac{\epsilon_{21}}{\epsilon_{32}} \tag{C.4}$$

and it should be positive and less than one to obtain the desired monotonic convergence. A Richardson extrapolation can be used when monotonic convergence is achieved:

$$f_{exact} \approx f_1 + \frac{\epsilon_{21}}{r^p - 1} \tag{C.5}$$

From equation (C.5), the extrapolated value is varied by different choice the order p. According to Stern *et al.* [43] the order-of-accuracy can be estimated by using the following equation:

$$p = \frac{\ln\left[\frac{\epsilon_{32}}{\epsilon_{21}}\right]}{\ln[r]} \tag{C.6}$$

Table C.1 shows the mesh dependency study results of all the computations. The first three correspond to the simulations of a single vortex generator on a flat plate with different device angles of the *Chapters 5, 6, 7 and 8*. The last two correspond to the simulations of *Chapter 9 and 10*, respectively.

	Mesh			**Richardson E.**		
AOA (β)	h_3	h_2	h_1	**RE**	**p**	**R**
20°	0.980	0.765	0.750	0.751	3.841	0.069
25°	0.920	0.720	0.691	0.695	2.785	0.145
30°	0.910	0.720	0.671	0.688	1.955	0.257
35°	0.890	0.701	0.662	0.672	2.276	0.206
Twin-Plate	0.995	0.931	0.926	0.926	3.678	0.078
NACA0012	0.985	0.840	0.831	0.831	3.858	0.069

TABLE C.1: Mesh-dependency study results.

Appendix D

BAY model

The BAY source term model developed by Bender *et al.* [22] was design for simulating vane vortex generators in a finite volume Navier-Stokes codes. The model was incorporated into the EllipSys CFD code as a source term model in the momentum and energy equations. This model applies a force normal to the local flow direction and parallel to the surface, see Figures D.1 and D.2. This force simulates the side force generated by a vane vortex generator. This modes adds a source term and it is applied in a region of cells located at the VG position and the VG geometry is not represented. Bender *et al.* designed this model based on the Joukowski lift theorem and on the thin airfoil theory to model the effect of VGs. Modelling the effect of a vortex generator using a very fine mesh can be replaced by adding forces in the region where the VG is located.

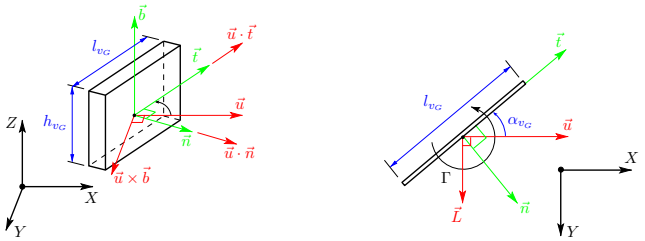

(a) (b)

FIGURE D.1: BAY model source term vectors

Considering a rectangular vortex generator the lift forces on the VG can be estimated by:

$\overrightarrow{L} \equiv$ Lift Force on the VG (Joukovski lift th x span of VG "h")

$$\overrightarrow{L} = \rho(\vec{u} \times \vec{b})\Gamma h_{VG} \tag{D.1}$$

$\vec{b}, \vec{n}, \vec{t} \equiv$ Unit Vectors $\rho =$density $\Gamma =$Circulation
$\vec{u} \equiv$ Local velocity vector $\vec{b} = \vec{n} \times \vec{t}$

The direction of the force is defined as the produt of the local velocity $\vec{u}$ and the unit vector $\vec{b}$ along the VG. The normal and tangential vectors of the VG are represented by $\vec{n}$ and $\vec{t}$, respectively.

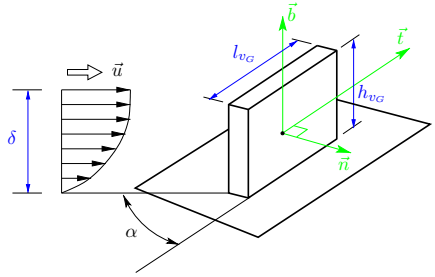

FIGURE D.2: 3D view of forces on a rectangular VG.

The local angle of attack can be calculated by:

$$\sin\alpha = \frac{\vec{u}.\vec{n}}{\parallel \vec{u} \parallel} \Rightarrow If \;\; \alpha \ll 1 \Rightarrow \alpha \cong \frac{\vec{u}.\vec{n}}{\parallel \vec{u} \parallel} \quad \text{(D.2)}$$

According to 2D airfoil theory [Joukovsky]$\Rightarrow \Gamma = \alpha \parallel \overrightarrow{u} \parallel l_{VG}$

$\overrightarrow{L} = \pi\rho(\vec{u} \times \vec{b})(\vec{u}.\vec{n})S_{VG}$ $S_{VG} \equiv$ plan parallel surface ($l_{VG} \times h_{VG}$)

$\overrightarrow{L}_{cell} = \pi\rho(\vec{u} \times \vec{b})(\vec{u}.\vec{n})S_{VG}\frac{V_{cell}}{V_s}$ $V_s \equiv$ Total volume

According to Bender *et al.* [22] this new term is introduced: $\left(\frac{\vec{u}.\vec{t}}{\|\vec{u}\|}\right)$

$$\overrightarrow{L}_{cell} = c\rho(\vec{u} \times \vec{b})(\vec{u}.\vec{n}) \left(\frac{\vec{u}.\vec{t}}{\parallel \vec{u} \parallel}\right) S_{VG}\frac{V_{cell}}{V_s} \quad \text{(D.3)}$$

When the BAY model is applied a calibration process is needed together with a mesh resolved VG model as a reference for the calibration. Hence, the constant c of the equation D.3 is a relaxation parameter used to perform the model. This parameter is chosen such that the results of the simulations with the distributed force fit the results of the corresponding computations of the mesh-resolved VG. In this research rentangular vortex generators is considered, see Figure 5.3. The calibration of the BAY model in this case is described in *Chapter 5*.

Bibliography

[1] Øye S. The effect of vortex generators on the performance of the Elkraft 1000 kw turbine. 9th IEA Symposium on Aerodynamics of Wind Turbines, Stockholm, Sweden, ISSN 0590-8809, 1995.

[2] van Rooij R.P.J.O.M. and Timmer W. A. Roughness sensitivity considerations for thick rotor blade airfoils. *Journal of Solar Energy Engineering-Transactions of the ASME*, 125(4):468–478, 2003.

[3] Velte C.M. *Characterization of vortex generator induced flow.* Phd thesis, Technical University of Denmark, Lyngby, Denmark, 2009.

[4] Velte C.M. A vortex generator flow model based on self-similarity. *AIAA Journal (ISSN: 0001-1452)*, 51(2):526–529, 2012.

[5] Miller G.E. Comparative performance tests on the Mod-2, 2.5-MW wind turbine with and without vortex generators. Cleveland, OH, United States, 8-10, 1984. DOE/NASA Workshop on Horizontal Axis Wind Turbine Technology.

[6] Rao D.M. and Kariya T.T. Boundary-layer submerged vortex generators for separation control - an exploratory study. *AIAA/ASME/SIAM/APS 1st National Fluid Dynamics Congress, Cincinnati, OH*, 88:25–28, July 1988.

[7] Mohamed Gad el Hak. *Flow Control: Passive, Active, and Reactive Flow Management.* Cambridge University Press, 1st edition edition, 2007.

[8] Lin J.C., Robinson S. K., McGhee R. J., and Valarezo W.O. Separation control on high-lift airfoils via micro vortex generators. *Journal of aircraft*, 27(5):503–507, 1994.

[9] Anderson B.H. The aerodynamic characteristics of vortex ingestion for the fla-18 inlet duct. 29th Aeroespace Sciences Meeting, Nevada, 1991.

[10] Taylor H.D. The elimination of diffuser separation by vortex generators. Research department report no. r-4012-3, United Aircraft Corporation, East Hartford, Connecticut, 1947.

[11] Taylor H.D. Application of vortex generator mixing principles to diffusers. Research department concluding report no. r-15064-5, United Aircraft Corporation, East Hartford, Connecticut, 1948.

[12] Taylor H.D. Summary report on vortex generators. Research department report no. r-05280-9, United Aircraft Corporation, East Hartford, Connecticut, 1950.

[13] Peppler IL. *From the ground up.* Aviation Publishers, Co. Limited, 1996.

[14] Lin J.C. and Howard F.G. Turbulent flow separation control through passive techniques. volume 89-0976. AIAA 2nd Shear Flow Conference, 1989.

[15] Kerho M., Huctcherson S., Blackwelder R. F., and Liebeck R. H. Vortex generators used to control laminar separation bubbles. *Journal of aircraft*, 30(3):315–319, 1993.

[16] Lin S., Robinson K., and McGhee R.J. Separation control on high-lift airfoils via micro vortex generators. *Journal of aircraft*, 27(5):503–507, 1994.

[17] Wendt B.J. Parametric study of vortices shed from airfoil vortex generators. *AIAA Journal*, 42:2185–2195, 2004.

[18] Schubauer G.B. and Spangenber W.G. Forced mixing in boundary layers. In *Journal of Fluid Mechanics* G.B. and W.G. [64], pages 10–32.

[19] Bragg M. B. and Gregorek G.M. Experimental study of airfoil performance with vortex generators. *Journal of Aircrafts*, 24(5):305–309, 1987.

[20] Godard G. and Stanislas M. Control of a decelerating boundary layer. Part 1: Optimization of passive vortex generators. *Aerospace Science and Technology*, 10: 181–191, 2006. DOI: 10.1016/j.ast.2005.11.007.

[21] Reck M. *Computational fluid dynamics, with dattached eddy simulation and the immersed boundary technique, applied to oscilating airfoilds and vortex generators.* PhD thesis, Technical University of Denmark, Department of Mechanical Engineering., 2004.

[22] Bender E.E., Anderson B.H., and Yagle P.J. Vortex generator modeling for Navier-Stokes Codes. *American Soc.of Mechanical Engineers FEDSM99-6929 New York*, 1999.

[23] Jirsek A. Vortex-generator model and its application to flow control. *Journal of Aircraft*, 42(6), 2005. Swedish Defence Research Agency FOI, SE-172 90 Stockholm, Sweden.

[24] Townsend A.A. The structure of turbulent shear flow. *London Cambridge University Press*, 1956.

[25] Harsha P.T. and Lee S.C. Correlation between turbulent shear stress and turbulent kinetic energy. *AAIA Journal*, 8, 1970.

[26] Patel V.C. and Scheuerer G. Calculations of two-dimensional near and far wakes. *AIAA Journal*, 20:900–907, 1982.

[27] Prabhu A. and Narasimha R. A. Turbulent non-equilibrium wakes. *J. Fluid Mechanics*, 54:1–17, 1972.

[28] Narasimha R. and Prabhu A. Equilibrium and relaxation in turbulent wakes. *J. Fluid Mechanics*, 54:19–38, 1972.

[29] Hebbar K.S. Mean and turbulence measurements in the boundary layer and wake of a symmetric aerofoil. *Experiments in Fluid Dynamics, Springer-Verlag*, 4:214–222, 1986.

[30] Wygnanski I., Champagne F., and Marasli B. On the large-scale structures in two-dimensional, small-deficit, turbulent wakes. *J. Fluid Mechanics*, 168:31–71, 1986.

[31] Fernández-Gámiz U. et al. Self-similarity and helical symmetry in vortex generator flow simulations. Torque 2012, The science of making torque from wind, Oldenburg, 2012.

[32] George W.K. The self-preservation of turbulent flows and its relation to initial conditions and coherent structures. *Advances in turbulence, (eds. Arndt R. Georg W.K.)*, pages 75–125, 1989.

[33] White F.M. *Viscous Fluid Flow.* McGraw-Hill, Singapore, third edition, 1991. pp. 470-481.

[34] Michelsen J.A. Basis3D- a platform for development of multiblock pde solvers. Technical report AFM 94-05, Technical University of Denmark, Dept. of Mechanical Engineering, 1992.

[35] Sørensen N.N. General purpose flow solver applied to flow over hills. Technical report risoe-r-827(en), Risoe National Laboratory, 1995.

[36] Velte C.M., Hansen M.O.L., and Okulov V.L. Helical structure of longitudinal vortices embedded in turbulent wall-bounded flow. *Journal of Fluid Mechanics*, 619:167–177, 2009.

[37] Sreenivasan K.R. and Narasimha R. Equilibrium parameters for two-dimensional turbulent wakes. *Journal of Fluids Engineering*, 104, 1982.

[38] Dudek J. Empirical model for vane-type vortex generators in a Navier-Stokes Code. *AIAA Journal*, 44(8), 2011. NASA John H. Glenn Research Center at Lewis Field, Cleveland, Ohio.

[39] Dudek J. Vortex generators in a Navier-Stokes Code. *AIAA Journal*, 49(4), 2011. NASA John H. Glenn Research Center at Lewis Field, Cleveland, Ohio.

[40] Fernández U., Réthoré P.-E., Sørensen N.N., Velte C.M., Zahle F., and Egusquiza E. Comparison of four different models of vortex generators. European Wind Energy Conference, Article in Proceedings of EWEC 2012, 2012.

[41] Liu J., Piomelli U., and Spalart P.R. Interaction between a spatially growing turbulent boundary layer and embedded streamwise vortices. *Journal of Fluid Mechanics*, 326:151–179, 1996.

[42] Richardson L. F. and Gaunt J. A. The deferred approach to the limit. Part I. single lattice. Part II. Interpenetrating lattices. *Philosophical Transactions of the Royal Society of London. Series A.*, 226:299–361, 1927.

[43] Stern F. et al. Verification and validation of the cfd simulations. Technical report, The University of Iowa, 1999.

[44] Réthoré P.-E. Søensen N. N. and Zahle F. Validation of an actuator disc model. Article in Proceedings EWEC, 2010.

[45] Réthoré P.-E. and Sørensen N.N. A discreet force allocation algorithm for modeling wind turbines in CFD. *Wind Energy Journal*, 15(7):915–926, 2012.

[46] Troldborg N., Zahle F., Réthoré P.-E., and Sørensen N.N. Comparison of the wake of different types of wind turbine CFD models. *AIAA*, 2012-0237. DOI: 10.2514/6.2012-237.

[47] Okulov V.L. Technical University of Denmark, Lyngby, Denmark. Private communication, 2012.

[48] Alekseenko S.V., Kuibin P.A., and Okulov V.L. *Theory of concentrated vortices*. Number ISBN 978-3-540-73375-1. Springer-Verlag, Heidelberg, Chap. 1, 1st edition, 2007.

[49] Khosla P.K. and Rubin S.G. A diagonally dominant second-order accurate implicit scheme. *Computer Fluids*, pages 207–209, 1974.

[50] Menter F.R. Zonal two equation k- turbulence model for aerodynamic flows. *AIAA Journal*, 93-2906, 1993.

[51] Smith F.T. Theoretical prediction and design for vortex generators in turbulent boundary layers. *Journal of Fluid Mechanics*, 270:91–131, 1994.

[52] Fernández-Gámiz U., Velte C.M., and Egusquiza E. Numerical simulations on a twin plate wake. Lisbon, 2013. International Congress on Energy and Environment (CIIEM).

[53] Sreenivasan K.R. Approach to self-preservation in plane turbulent wakes. *AIAA Journal*, 19:1365–1367, 1981.

[54] Marvin J.G. Turbulance modeling for computational aerodynamics. *AIAA Journal*, 21:941–955, 1983.

[55] R. Chevray and L.S.G. Kovasznay. Turbulance measurements in the wake. *AIAA Journal*, 7:1641–1643, 1969.

[56] Hebbar K. S. Experimental study of incompressible mean and turbulence flow fields on and behind a symmetric aerofoil. Technical report, Technical Memorandum AE-TM-4-81, National Aeronautical Laboratory, Bangalore, India, 1981.

[57] Michelsen J.A. Block structured multigrid solution of 2D and 3D elliptic PDE's. Technical report afm 94-05, Technical University of Denmark, Dept. of Mechanical Engineering, 1994.

[58] Rhie C.M. A numerical study of the flow past an isolated airfoild with separation. Phd thesis, University of Illinois, 1981.

[59] Potter M. and Wiggert D.C. *Fluid Mechanics*. McGraw-Hill (USA), 2008.

[60] Aris R. *Vectors, Tensors, and the basic Equations of Fluid Mechanics*. Dover Publications, 1989.

[61] Anderson J.D. Jr. *Computational Fluid Dynamics. The Basics with Applications*. McGraw-Hill, 1995.

[62] Menter F.R. Review of the shear-stress transport turbulence model experience from a industrial perspective. *Int. J. of Comp. Fluid Dynamics*, 23(1-4):277–303, 2009.

[63] Roache PJ. Perspective: A method for uniform reporting of grid refinement studies. *Journal of Fluid Engineering*, 116(3):405–41, 1994.

[64] Schubauer G.B. and Spangenber W.G. Forced mixing in boundary layers. *Journal of Fluid Mechanics*, 8(1):10–32, March 1960.